



1 **Sensitivity of cloud phase distribution to cloud microphysics and**  
2 **thermodynamics in simulated deep convective clouds and SEVIRI**  
3 **retrievals**

4 Cunbo Han<sup>1,2</sup>, Corinna Hoose<sup>1</sup>, Martin Stengel<sup>3</sup>, Quentin Coopman<sup>4</sup>, Andrew Barrett<sup>1</sup>

5

6 1. Institute of Meteorology and Climate Research (IMK-TRO), Karlsruhe Institute of  
7 Technology, Karlsruhe, Germany

8 2. Now at State Key Laboratory of Tibetan Plateau Earth System, Environment and  
9 Resources (TPESER), Institute of Tibetan Plateau Research, Chinese Academy  
10 of Sciences, Beijing, China

11 3. Deutscher Wetterdienst (DWD), Offenbach, Germany

12 4. Department of Atmospheric and Oceanic Sciences, McGill University, Montreal,  
13 Canada

14

15

16

17

18

19 Correspondence to: Cunbo Han ([cunbo.han@hotmail.com](mailto:cunbo.han@hotmail.com)) and Corinna Hoose  
20 ([corinna.hoose@kit.edu](mailto:corinna.hoose@kit.edu))

21

22



23 **Abstract:**

24 The formation of ice in clouds is an important process in mixed-phase clouds, and  
25 the radiative properties and dynamical developments of clouds strongly depend on  
26 their partitioning between liquid and ice phases. In this study, we investigate the  
27 sensitivities of the cloud phase to ice-nucleating particle (INP) concentration and  
28 thermodynamics. Experiments are conducted using the ICOSahedral Nonhydrostatic  
29 model (ICON) at the convection-permitting resolution of about 1.2 km on a domain  
30 covering significant parts of central Europe, and are compared to two different  
31 retrieval products based on SEVIRI measurements. We select a day with several  
32 isolated deep convective clouds, reaching a homogeneous freezing temperature at  
33 the cloud top. The simulated cloud liquid pixel number fractions are found to  
34 decrease with increasing INP concentration both within clouds and at the cloud top.  
35 The decrease in cloud liquid pixel number fraction is not monotonic but is stronger in  
36 high INP cases. Cloud-top glaciation temperatures shift toward warmer temperatures  
37 with increasing INP concentration by as much as 8 °C. Moreover, the impact of INP  
38 concentration on cloud phase partitioning is more pronounced at the cloud top than  
39 within the cloud. Moreover, initial and lateral boundary temperature fields are  
40 perturbed with increasing and decreasing temperature increments from 0 to +/-3K  
41 and +/-5K between 3 and 12 km. Perturbing the initial thermodynamic state is also  
42 found to affect the cloud phase distribution systematically. However, the simulated  
43 cloud-top liquid number fraction, diagnosed using radiative transfer simulations as  
44 input to a satellite forward operator and two different satellite remote sensing  
45 retrieval algorithms, deviates from one of the satellite products regardless of  
46 perturbations in the INP concentration or the initial thermodynamic state for warmer  
47 sub-zero temperatures, while agreeing with the other retrieval scheme much better,  
48 in particular for the high INP and high convective available potential energy (CAPE)  
49 scenarios. Perturbing the initial thermodynamic state, which artificially increases the  
50 instability of the mid- and upper-troposphere, brings the simulated cloud-top liquid  
51 number fraction closer to the satellite observations, especially in the warmer mixed-  
52 phase temperature range.

53

54 **Keywords:** Mixed-phase clouds, deep convection, INP, thermodynamics, satellite  
55 forward operator, remote-sensing retrieval algorithms



56

57 **Key points:**

- 58 1. Cloud properties are retrieved using a satellite forward operator and remote  
59 sensing retrieval algorithms with ICON simulations as input. To our knowledge,  
60 it is the first time this approach has been used to retrieve cloud phase and other  
61 microphysical variables.
- 62 2. Glaciation temperature shifts towards a warmer temperature with increasing  
63 INP concentration both within the cloud and at the cloud top. Initial  
64 thermodynamic states affect the cloud phase distribution significantly as well.
- 65 3. Simulated cloud-top pixel number fraction matches the satellite observations in  
66 the high INP and high CAPE scenarios.

67



68 **1. Introduction**

69 In the temperature range between 0 and  $-38^{\circ}\text{C}$ , ice particles and supercooled liquid  
70 droplets can coexist in mixed-phase clouds. Mixed-phase clouds are ubiquitous in  
71 Earth's atmosphere, occurring at all latitudes from the poles to the tropics. Because  
72 of their widespread nature, mixed-phase processes play a critical role in the life cycle  
73 of clouds, precipitation formation, cloud electrification, and the radiative energy  
74 balance on both regional and global scales ([Korolev et al., 2017](#)). Deep convective  
75 clouds are always mixed-phase clouds, and their cloud tops reach the homogeneous  
76 freezing temperature,  $-38^{\circ}\text{C}$ , in most cases. Despite the importance of mixed-phase  
77 clouds in shaping global weather and climate, microphysical processes for mixed-  
78 phase cloud formation and development are still poorly understood, especially ice  
79 formation processes. It is not surprising that the representation of mixed-phase  
80 clouds is one of the big challenges in weather and climate models ([McCoy et al.,](#)  
81 [2016](#); [Korolev et al., 2017](#); [Hoose et al., 2018](#); [Takeishi and Storelvmo, 2018](#); [Vignon](#)  
82 [et al., 2021](#); [Zhao et al., 2021](#)).

83  
84 The distribution of cloud phase has been found to impact cloud thermodynamics and  
85 Earth's radiation budget significantly ([Korolev et al., 2017](#); [Matus and L'Ecuyer,](#)  
86 [2017](#); [Hawker et al., 2021](#)). The freezing of liquid droplets releases latent heat and  
87 hence affects the thermodynamic state of clouds. Moreover, distinct optical  
88 properties of liquid droplets and ice particles exert different impacts on cloud's  
89 shortwave and longwave radiation. Observational studies reveal that the cloud phase  
90 distribution is highly temperature-dependent and influenced by multiple factors, for  
91 example, cloud type and cloud microphysics ([Rosenfeld et al., 2011](#); [Coopman et al.,](#)  
92 [2020](#)). Analyzing passive satellite observations of mixed-phase clouds over the  
93 Southern Ocean, [Coopman et al. \(2021\)](#) found that cloud ice fraction increases with  
94 increasing cloud effective radius. Analysis of both passive and active satellite  
95 datasets reveals an increase in supercooled liquid fraction with cloud optical  
96 thickness ([Bruno et al., 2021](#)).

97  
98 A number of in-situ observations of mixed-phase clouds have been made in the past  
99 several decades, covering stratiform clouds ([Pinto, 1998](#); [Korolev and Isaac, 2006](#);  
100 [Noh et al., 2013](#)) and convective clouds ([Rosenfeld and Woodley, 2000](#); [Stith et al.,](#)



101 [2004](#); [Taylor et al., 2016](#)). Aircraft-based observations of mixed-phase clouds  
102 properties reveal that the frequency distribution of the ice water fraction has a U-  
103 shape, with the occurrence of mixed-phase clouds decreasing toward lower  
104 temperatures ([Korolev et al., 2003](#); [Field et al., 2004](#); [Korolev et al., 2017](#)). These  
105 findings are very useful constraints of numerical models ([Lohmann and Hoose, 2009](#);  
106 [Grabowski et al., 2019](#)). However, in-situ observations of mixed-phase cloud  
107 microphysics are technically difficult and sparse in terms of spatial and temporal  
108 coverage. Thus, understanding ice formation processes and determining the  
109 climatological significance of mixed-phase clouds have proved difficult using existing  
110 in-situ observations only.

111

112 Both observations and simulations reveal that INPs impact deep convective cloud  
113 properties including the persistence of deep convective clouds and precipitation  
114 ([Twohy, 2015](#); [Fan et al., 2016](#)). Satellite observations indicate that dust serves as  
115 effective INPs in the Saharan air layer, promotes the heterogeneous ice nucleation  
116 process, shifts the precipitation size distribution from large to small raindrops in deep  
117 convective clouds, and ultimately reduces precipitation ([Min et al., 2009](#)). However,  
118 the convection-permitting simulations by [van den Heever et al. \(2006\)](#) showed that  
119 convective precipitation increases with increasing INPs. Moreover, some simulation  
120 studies argue that dust aerosols acting as INPs have hardly any effect on convective  
121 precipitation although they significantly impact cloud microphysical properties ([Fan et](#)  
122 [al., 2010](#); [Fan et al., 2016](#)). [Li and Min \(2010\)](#) suggested that the impacts of INPs on  
123 deep convective precipitation systems highly depend on the precipitation type.

124 Although the effects of INPs on convective precipitation are not conclusive, it is  
125 certain that the interactions between convective clouds and INPs affect cloud  
126 microphysical properties and hence cloud phase distributions. In addition, previous  
127 numerical modeling studies on cloud-aerosols interactions have focused on  
128 influences of aerosols acting as cloud condensation nuclei (CCN) ([Fan et al., 2016](#)),  
129 which are linked to the ice phase e.g. through impacts on the riming efficiency  
130 ([Barrett and Hoose, 2023](#)). Given the limited knowledge on ice formation in deep  
131 convective clouds and significant uncertainties in ice nucleation parameterizations, it  
132 is necessary to conduct sensitivity simulations to investigate how ice formation  
133 processes are influenced by INP concentrations and thermodynamic states in deep  
134 convective clouds.



135

136 In this study, with the help of realistic convection-permitting simulations using two-  
137 moment microphysics, we address how and to what extent INP concentration and  
138 thermodynamic state affect the in-cloud and cloud-top phase distributions in deep  
139 convective clouds. In particular, cloud properties are retrieved using a satellite  
140 forward operator and remote sensing retrieval algorithms with radiative transfer  
141 simulations as input for a fair comparison to observations from SEVIRI. A similar  
142 strategy was used by [Kay et al. \(2018\)](#) for the evaluation of precipitation in a climate  
143 model with CloudSat observations and termed “scale-aware and definition-aware  
144 evaluation”. [Stengel et al. \(2020\)](#) applied a cloud classification algorithm developed  
145 for satellite observations to model simulated brightness temperatures in a similar  
146 manner. This method allows us to compare model simulated cloud properties with  
147 remote sensing cloud products directly, and is, to our knowledge, the first time this  
148 approach is used for the cloud phase and related microphysical variables.

149

150 This paper is structured as follows: In section 2, we introduce our model setups and  
151 the experiment design, the satellite forward operator, remote sensing retrieval  
152 algorithms, and datasets. Simulation results for the sensitivity experiments are  
153 shown in section 3. Section 4 presents discussions; and we summarize the study  
154 and draw conclusions in section 5.

## 155 **2. Data and Method**

### 156 **2.1. Model description**

157 The Icosahedral Nonhydrostatic (ICON) model ([Zängl et al., 2015](#)) is a state-of-the-  
158 art unified modeling system offering three physics packages, which are dedicated to  
159 numerical weather prediction (NWP), climate simulation, and large-eddy simulation.  
160 ICON is a fully compressible model and has been developed collaboratively between  
161 the German Weather Service (DWD), Max Planck Institute for Meteorology, German  
162 Climate Computing Center (DKRZ), and Karlsruhe Institute of Technology (KIT). In  
163 order to maximize the model performance and to remove the singularity at the poles,  
164 ICON solves the prognostic variables suggested by [Gassmann and Herzog \(2008\)](#),  
165 on an unstructured triangular grid with C-type staggering based on a successive  
166 refinement of a spherical icosahedron ([Wan et al., 2013](#)). Governing equations are



167 described in [Wan et al. \(2013\)](#) and [Zängl et al. \(2015\)](#). The DWD has operated the  
168 ICON model at a spatial resolution of about 13 km on the global scale since January  
169 2015. In the global ICON, the higher-resolution ICON-EU (resolution 7 km) nesting  
170 area for Europe has been embedded since July 2015. In this study, ICON-2.6.4 with  
171 the NWP physics package is used and initial and lateral boundary conditions are  
172 provided by the ICON-EU analyses.

173

174 For cloud microphysics, we use an updated version of the two-moment cloud  
175 microphysics scheme developed by [Seifert and Beheng \(2006\)](#). The two-moment  
176 scheme predicts the number and mass mixing ratios of two liquid (cloud and rain)  
177 and four solid (ice, graupel, snow, and hail) hydrometers. The cloud condensation  
178 nuclei (CCN) activation is described following the parameterization developed by  
179 [Hande et al. \(2016\)](#). Homogeneous freezing, including freezing of liquid water  
180 droplets and liquid aerosols, is parametrized according to [Kärcher et al. \(2006\)](#).  
181 Heterogeneous ice nucleation, including the immersion and deposition modes, is  
182 parameterized as a function of temperature- and ice supersaturation-dependent INP  
183 concentration ([Hande et al., 2015](#)). The INP concentration due to immersion  
184 nucleation is described as the following equation:

$$185 \quad C_{INP}(T_K) = A \times \exp[-B \times (T_K - T_{min})^C] \quad (1)$$

186 where  $T_K$  is the ambient temperature in Kelvin;  $A$ ,  $B$ , and  $C$  are fitting constants with  
187 different values to represent seasonally varying dust INP concentrations. The  
188 parameterization for deposition INPs is simply scaled to the diagnosed relative  
189 humidity with respect to ice ( $RH_{ice}$ ):

$$190 \quad C_{INP}(T_K, RH_{ice}) \approx C_{INP}(T_K) \times DSF(RH_{ice}) \quad (2)$$

$$191 \quad DSF(RH_{ice}) = a \times \arctan(b \times (RH_{ice} - 100) + c) + d \quad (3)$$

192 where  $C_{INP}(T_K)$  is given by Equation (1);  $a$ ,  $b$ ,  $c$ , and  $d$  are constants. More details  
193 are found in [Hande et al. \(2015\)](#).

## 194 2.2. Simulation setup and sensitivity experiments

195 In this study, the setup consists of two different domains with one-way nesting  
196 covering a major part of central Europe (Figure 1). The horizontal resolution for the  
197 nested domains is halved from 2400 m to 1200 m in the innermost domain, and the  
198 time steps for the two domains are 12 s and 6 s, respectively. 150 vertical levels are



199 used, with a grid stretching towards the model top at 21 km. The vertical resolution is  
200 the same for all horizontal resolutions and the lowest 1000 m encompass 20 layers.  
201 A 1-D vertical turbulence diffusion and transfer scheme is used for the 2400 m and  
202 1200 m resolutions, referred to as numerical weather prediction (NWP) physics.  
203 Deep convection is assumed to be explicitly resolved, while shallow convection is  
204 parameterized for both domains. The simulations are initialized at 00:00 UTC on the  
205 study day from ICON-EU analyses and integrated for 24 hours. At the lateral  
206 boundaries of the outer domain, the simulation of the model is updated with 3-hourly  
207 ICON-EU analyses. The nested domains are coupled online, and the outer domain  
208 provides lateral boundary conditions to the inner domain.

209

210 In nature, INP concentration varies across multiple orders of magnitude ([Hoose and](#)  
211 [Möhler, 2012](#); [Kanji et al., 2017](#)). Thus, in our sensitivity experiments, heterogeneous  
212 ice formation was scaled by multiplying the default INP concentration (Equation (1))  
213 with a factor of  $10^{-2}$ ,  $10^{-1}$ ,  $10^1$ ,  $10^2$ ,  $10^3$  for both immersion freezing and deposition ice  
214 nucleation. Together with a case with default INP concentration (case CTRL) and  
215 one case switching off the secondary-ice production via rime-splintering process (the  
216 so called Hallet-Mossop process), 7 cases were created in total to investigate the  
217 impact of primary and secondary ice formation on cloud phase distribution in deep  
218 convective clouds.

219

220 In order to assess the sensitivity of the cloud phase to thermodynamics, initial and  
221 lateral boundary temperature fields are modified with increasing and decreasing  
222 temperature increments, named experiments INC and DEC, respectively. The  
223 temperature increments are linearly increasing/decreasing from 0 to +/-3K and +/-5K  
224 between 3 and 12 km, creating 4 sensitivity experiments DEC03, DEC05, INC03,  
225 and INC05. Above 12 km, the increment is constant up to the model top. Initial  
226 temperature profiles are shown in Figure 2. The increasing or decreasing  
227 environmental temperature leads to changes in the lapse rate and the stability of the  
228 atmosphere, and hence results in decrease or increase in the convective available  
229 potential energy (CAPE), respectively ([Barthlott and Hoose, 2018](#)). Thus, the CAPE  
230 increases monotonically from case INC05 (spatial-averaged CAPE at 9:00 UTC: 413  
231  $\text{J kg}^{-1}$ ) to case CTRL ( $724 \text{ J kg}^{-1}$ ) and finally to DEC05 ( $1235 \text{ J kg}^{-1}$ ). Note that the  
232 relative humidity increases/decreases with decreasing/increasing temperature as the





233 specific humidity is unperturbed. The perturbations of INP concentration and  
234 initial/lateral temperature profiles are motivated by [Hoose et al. \(2018\)](#) and [Barthlott  
235 and Hoose \(2018\)](#), respectively. Complementary to these earlier studies, we now  
236 investigate an ensemble of several deep convective clouds and focus on influences  
237 of INP and thermodynamics on cloud phase distribution. Short descriptions of all  
238 sensitivity experiments performed in this study are listed in Table 1.

### 239 **2.3. Satellite observations and retrieval algorithms**

240 The Spinning Enhanced Visible and Infrared Imager (SEVIRI) is a 12-channel imager  
241 on board the geostationary Meteosat Second Generation (MSG) satellites. SEVIRI  
242 has one high spatial resolution visible channel (HRV) and 11 spectral channels from  
243 0.6 to 14  $\mu\text{m}$  with a 15 min revisit cycle and a spatial resolution of 3 km at nadir  
244 ([Schmetz et al., 2002](#)). Based on the spectral measurements of SEVIRI, a cloud  
245 property data record, the CLAAS-2 dataset (CLOUD property dAtAset using SEVIRI,  
246 Edition 2), has been generated in the framework of the EUMETSAT Satellite  
247 Application Facility on Climate Monitoring (CM SAF) ([Benas et al., 2017](#)). CLAAS-2  
248 is the successor of CLAAS-1 ([Stengel et al., 2014](#)), for which retrieval updates have  
249 been implemented in the algorithm for the detection of clouds compared to CLAAS-1  
250 ([Benas et al., 2017](#)) with the temporal coverage being extended to 2004-2015.  
251 Retrieval algorithms for parameters that are important for this study are introduced  
252 below. Detailed descriptions for the retrieval algorithms are found in [Stengel et al.  
253 \(2014\)](#) and [Benas et al. \(2017\)](#) with the main features being summarized in the  
254 following.

255

256 The MSGv2012 software package is employed to detect clouds and their vertical  
257 placement ([Derrien and Le Gléau, 2005](#); [Benas et al., 2017](#)). Multi-spectral threshold  
258 tests, which depend on illumination and surface types, among other factors, are  
259 performed to detect cloud appearances. Each satellite pixel is assigned to categories  
260 of cloud-filled, cloud-free, cloud water contaminated, or snow/ice contaminated.  
261 Cloud top pressure (CTP) is retrieved with different approaches using input from  
262 SEVIRI channels at 6.2, 7.3, 10.8, 12.0, and 13.4  $\mu\text{m}$  ([Menzel et al., 1983](#); [Schmetz  
263 et al., 1993](#); [Stengel et al., 2014](#); [Benas et al., 2017](#)). Cloud top height (CTH) and  
264 cloud top temperature (CTT) are derived from CTP using ancillary data for



265 temperature and humidity profiles from ERA-Interim ([Dee et al., 2011](#)). The cloud top  
266 phase (CPH) retrieval is based on a revised version of the multispectral algorithm  
267 developed by [Pavolonis et al. \(2005\)](#). Clouds are categorized initially into six types,  
268 that are liquid, supercooled, opaque ice, cirrus, overlap, and overshooting.  
269 Subsequently, the binary cloud phase (liquid or ice) is generated based on the six  
270 categories ([Benas et al., 2017](#)). Cloud optical and microphysical properties are  
271 retrieved using the Cloud Physical Properties (CPP) algorithm ([Roebeling et al.,](#)  
272 [2006](#)). SEVIRI visible (0.6  $\mu\text{m}$ ) and near-infrared (1.6  $\mu\text{m}$ ) measurements are used  
273 to calculate cloud optical thickness (COT) and cloud particle effective radius ( $r_e$ ) by  
274 applying the [Nakajima and King \(1990\)](#) approach in the CPP algorithm ([Stengel et](#)  
275 [al., 2014](#); [Benas et al., 2017](#)). Liquid water path (LWP) and ice water path (IWP) are  
276 then computed as a function of liquid/ice water density, COT, and  $r_e$  of cloud water  
277 and cloud ice following the scheme developed by [Stephens \(1978\)](#).

278

279 In this study we used instantaneous CLAAS-2 data with temporal resolution of 15  
280 minutes and on native SEVIRI projection and resolution. In addition to the CLAAS-2  
281 dataset, the recently developed software suite SEVIRI\_ML (Philipp and Stengel, to  
282 be submitted) was applied to the SEVIRI measurements to obtain cloud top phase  
283 and cloud top temperature for the selected case. SEVIRI\_ML uses a machine  
284 learning approach calibrated against CALIOP. One feature of the SEVIRI\_ML is that  
285 it also provides pixel-based uncertainties such that values with low reliability can be  
286 filtered out.

#### 287 **2.4. Satellite forward operators**

288 In order to compare simulation results and satellite observations directly, SEVIRI-like  
289 spectral reflectance and brightness temperatures are calculated using the radiative  
290 transfer model for TOVS (RTTOV, v12.3) ([Saunders et al., 2018](#)). RTTOV is a fast  
291 radiative transfer model for simulating top-of-atmosphere radiances from passive  
292 visible, infrared, and microwave downward-viewing satellite radiometers. It has been  
293 widely used in simulating synthetic satellite images and assimilating radiances in  
294 numerical models ([Saunders et al., 2018](#); [Pscheidt et al., 2019](#); [Senf et al., 2020](#);  
295 [Geiss et al., 2021](#); [Rybka et al., 2021](#)).

296



297 In this work, ICON simulated surface skin temperature, near-surface pressure,  
298 temperature, specific humidity, wind velocity, total liquid water content, total ice water  
299 content, and effective radius of cloud liquid and cloud ice are used as input to drive  
300 the RTTOV model. Before inputting to the RTTOV model, ICON simulations are  
301 remapped onto SEVIRI's full disc coordinate. Brightness temperatures from 8  
302 channels (at 3.9, 6.2, 7.3, 8.7, 9.7, 10.8, 12.0, and 13.4  $\mu\text{m}$ ) and reflectance from 3  
303 channels (at 0.6, 0.8, and 1.6  $\mu\text{m}$ ) simulated by the RTTOV model are used as input  
304 to run the remote sensing retrieval algorithms to derive CLAAS-2-like and  
305 SEVIRI\_ML-like retrievals, named ICON\_RTTOV\_CLAAS-2 and  
306 ICON\_RTTOV\_SEVIRI\_ML products, respectively.

## 307 **2.5. Synoptic overview**

308 The day 06 June 2016 was selected to analyze, which was dominated by  
309 summertime deep convection located in central Europe. The synoptic forcing was  
310 weak on the day, and convection was triggered mainly by local thermal instabilities.  
311 The day has been discussed frequently in previous studies in terms of convection  
312 triggering, cloud microphysics, and its parameterizations ([Keil et al., 2019](#); [Geiss et  
313 al., 2021](#)).

## 314 **3. Results and discussion**

315 Perturbing INP concentration and temperature profiles directly affects microphysical  
316 and thermodynamic processes of the developing deep convective clouds, and hence  
317 impact in-cloud and cloud-top phase distributions. The following section shows  
318 results and discussions on the sensitivities of cloud phase and cloud microphysics to  
319 INP concentration and thermodynamic perturbations.

### 320 **3.1. Spatial distribution of cloud properties**

321 Before analyzing the results of sensitivity experiments, retrieved cloud properties via  
322 RTTOV and the CLAAS-2 retrieval scheme for the CTRL case are compared to  
323 CLAAS-2 products. Spatial distributions of derived LWP, IWP, and COT at 13:00  
324 UTC of the CTRL case and CLAAS-2 satellite observation are shown in Figure 3.  
325 Discrepancies are found between ICON simulation and CLAAS-2 satellite  
326 observations in terms of spatial coverage and intensity. The ICON simulation



327 overestimates the cloud coverage of low-level liquid clouds compared to CLAAS-2  
328 satellite observations, while LWP derived from the ICON simulation (case CTRL) is  
329 smaller and more homogeneously distributed than that from the CLAAS-2  
330 observation (Figure 3a and 3b). The spatial distributions of IWP and COT represent  
331 the approximate location and spatial extension of deep convective clouds in this  
332 study. The ICON simulation could reproduce cores of deep convective clouds of a  
333 number and spacing comparable to observations, while the spatial extension and  
334 intensity of individual deep convective clouds are not simulated very well by the  
335 ICON model. The ICON simulation underestimates the spatial extension of deep  
336 convective clouds but overestimates IWP and COT outside the convective cores  
337 compared to the CLAAS-2 observation (Figure 3c-f). Overall, the simulated clouds  
338 appear to be too homogeneous without sufficient internal structure. [Geiss et al.](#)  
339 [\(2021\)](#) also reported significant deviations between model simulations and satellite  
340 observations. Moreover, [Geiss et al. \(2021\)](#) concluded that the primary source of  
341 deviations is mainly from model physics, especially model assumptions on subgrid-  
342 scale clouds.

### 343 **3.2. Sensitivity of microphysical properties to INP perturbation**

344 Perturbing INP concentration results in a direct influence on the heterogeneous  
345 freezing processes and hence impacts on cloud microphysical properties.  
346 Systematic variations have been found in the spatial- and time-averaged profiles of  
347 mass mixing ratios of cloud hydrometeors as shown in Figure 4. All profiles  
348 discussed here are averaged over cloudy pixels (defined as having a condensed  
349 mass of cloud water plus cloud total cloud ice greater than a threshold of  $1.0 \times 10^{-5}$  kg  
350  $\text{kg}^{-1}$ ) and over the time period from 9:00 to 19:00 UTC, when convection was well  
351 developed. The mass concentration of ice crystals decreases with increasing INP  
352 concentration (Figure 4a). However, the mass concentration of snow, graupel, and  
353 rainwater increase with increasing INP concentration, especially in the high INP  
354 concentration cases (cases  $A \times 10^2$  and  $A \times 10^3$ ).

355

356 In order to further reveal why ice crystal mass concentration decreases with  
357 increasing INP concentration, we investigate process rates related to ice particle  
358 nucleation and growth. Figure 5 shows spatial- and time-averaged (from 9:00 to



359 19:00 UTC) profiles of process rates for homogeneous freezing, heterogeneous  
360 freezing, secondary ice production via the rime-splintering process, cloud droplets  
361 rimed with ice crystals, rain droplets rimed with ice crystals, and collection between  
362 ice and ice crystals. Heterogeneous freezing (Figure 5a) includes processes of  
363 immersion freezing, deposition ice nucleation, and immersion freezing of liquid  
364 aerosols ([Kärcher et al., 2006](#); [Hande et al., 2015](#)), see also equations (1) and (2).  
365 Process rates of heterogeneous freezing increase significantly with increasing INP  
366 concentration compared to the CTRL (Figure 5a). Compensating the change in  
367 heterogeneous freezing, process rates of homogeneous freezing decrease  
368 significantly with increasing INP concentration (Figure 5b). However, a decrease in  
369 INP concentration (compared to the CTRL) does not have a strong influence on the  
370 heterogeneous freezing mass rate, which is already low compared to the other  
371 processes in CTRL. Riming processes of cloud droplets and rain droplets onto ice  
372 crystals are greatly invigorated due to enhanced INP concentration (Figure 5d and  
373 5e). Moreover, process rates of secondary ice production due to rime-splintering are  
374 strengthened as well due to the increase in rimed ice, albeit much lower values.  
375 Figure 5f shows process rates of collection between ice and ice crystals. Process  
376 rates of collection between ice and ice particles increase with increasing INP  
377 concentration, especially in high INP concentration cases (cases  $A \times 10^2$  and  $A \times 10^3$ ).  
378 Process rates of collection of other ice particles all increase with increasing INP  
379 concentration, similar to the collection between ice and ice crystals (not shown). The  
380 increase in the riming of clouds and rain droplets onto ice crystals and collections  
381 between ice particles leads to the increase in the mass concentration of snow,  
382 graupel, and hail (Figure 4b and 4c). However, the total mass increase in snow,  
383 graupel, and hail do not outbalance the decrease in the mass concentration of ice  
384 crystals (Figure 4). The weakened homogeneous freezing is most likely the dominant  
385 factor leading to the decrease in ice mass concentration in high INP cases,  
386 considering the magnitude of the process rate of homogeneous freezing (Figure 5b).  
387 Supercooled liquid and cloud droplets have been converted into ice crystals before  
388 reaching the homogeneous freezing layer, leading to fewer supercooled droplets  
389 remaining for homogeneous freezing. Even though homogeneous freezing is  
390 weakened in high INP cases, the process rate of homogeneous freezing is still larger  
391 than heterogeneous freezing, which means homogeneous freezing is the dominant



392 ice formation process in the convective clouds discussed in this study. Moreover, the  
393 enhanced production of large ice particles (snow, graupel, and hail) in the highest  
394 INP case, which sediment more rapidly to lower levels, leads to increased surface  
395 precipitation by about 10% in the  $A \times 10^3$  case (not shown). Interestingly, ice crystal  
396 effective radius ( $r_e^{ice}$ ) increases monotonically with increasing INP concentration,  
397 especially in the mixed-phase layer (Figure 4e). [Zhao et al. \(2019\)](#) also reported an  
398 increased  $r_e^{ice}$  with polluted continental aerosols in their simulated moderate  
399 convection cases, and they attributed it to enhanced heterogeneous freezing and  
400 prolonged ice crystal growth at higher INP loading.

401

402 This competition between homogeneous and heterogeneous freezing has been  
403 discussed in previous studies ([Heymsfield et al., 2005](#); [Deng et al., 2018](#); [Takeishi  
404 and Storelvmo, 2018](#)). In contrast, simulations of mixed-phase moderately deep  
405 convective clouds by [Miltenberger and Field \(2021\)](#) indicate that cloud ice mass  
406 concentration increases with increasing INP concentration, which is in opposition to  
407 the findings in this work. The main reason is that the CTT is about  $-18^\circ\text{C}$  in  
408 [Miltenberger and Field \(2021\)](#)'s study, and heterogeneous freezing does not  
409 compete with homogeneous freezing. Thus, results on INPs effects on glaciation  
410 processes in convective clouds can be opposite under different conditions.

### 411 3.3. Cloud liquid mass fraction

412 Varying the INP concentration has a direct impact on the primary ice formation.  
413 Thus, it affects cloud liquid mass fraction within the clouds (directly for all cloudy  
414 layers where heterogeneous freezing is active and indirectly for warmer and colder  
415 temperatures) and at the cloud top. Cloud liquid mass fraction is defined as the ratio  
416 of mass mixing ratio between cloud droplets ( $q_c$ ) and the sum of cloud droplets and  
417 cloud ice crystals ( $q_i$ ). In-cloud liquid mass fraction, sampled at a time interval of 15  
418 minutes between 9:00 to 19:00 from all cloudy pixels, is shown as scatterplots  
419 versus temperature in Figure 6a-d. The corresponding frequencies of the occurrence  
420 of the temperature/liquid fraction bins are shown in Figure 6e-h. Similar analyses  
421 were made by [Hoose et al. \(2018\)](#), but for idealized simulations of deep convective  
422 clouds. In-cloud liquid mass fractions smaller than 0.5 are quite common already at  
423 temperature just below  $-3^\circ\text{C}$  except for the case without rime-splintering process



424 ( $A \times 10^0$ \_NSIP). The decrease in INP concentrations has limited effects on the in-  
425 cloud liquid mass fraction (Figure 6c and 6g), while a stronger influence has been  
426 found in the case with enhanced INP concentration (Figure 6d and 6h). The number  
427 of pixels having high liquid mass fraction values at temperatures lower than  $-30$  °C  
428 decreases with increasing INP concentration. In addition, more and more pixels  
429 having liquid mass fraction smaller than 0.5 appear with increasing INP  
430 concentration and the number of pure ice pixels increases with increasing INP  
431 concentration as well. This is because higher INP concentration intensifies the  
432 heterogeneous freezing processes (immersion freezing and deposition ice  
433 nucleation) and invigorates the rime-splintering process as well (will be discussed in  
434 section 3.3). Interestingly, at the lower end of the mixed-phase temperature range ( $-$   
435  $38 \sim -28$  °C), there are fewer pixels having high liquid mass fraction in the high INP  
436 case, and those remaining are mainly the ones at high vertical velocities (above  $\sim 10$   
437 m/s). This is probably because supercooled droplets are more easily frozen in high  
438 INP cases and stronger updrafts are needed to offset the Wegener-Begeron-  
439 Findeisen process to maintain the supersaturation with respect to water. Switching  
440 off the secondary ice production via rime-splintering process, pixels having a liquid  
441 mass fraction smaller than 0.9 are reduced significantly at temperatures between  $-$   
442  $10$  °C and  $0$  °C (Figure 6b and 6f).

443

444 At the cloud top (Figure 7), the number of pixels having a liquid mass fraction smaller  
445 than 0.5 increases with increasing INP concentration, which is the same as within  
446 the clouds. “Cloud top” is defined as the height of the uppermost cloud layer (which  
447 has a condensed mass of cloud water plus cloud total cloud ice greater than a  
448 threshold of  $1.0 \times 10^{-5}$  kg kg<sup>-1</sup>) in a pixel column. At the cloud top, the liquid mass  
449 fraction has a more polarized distribution, with either large values or small values,  
450 and intermediate values are less common than within the clouds. This is because the  
451 vertical velocities at the cloud top are significantly smaller compared to that within  
452 the cloud, which leads to a more efficient Wegener-Begeron-Findeisen process at  
453 the cloud top.



454 **3.4. Liquid cloud pixel number fraction**

455 Liquid cloud pixel number fractions are calculated differently for model simulations  
456 and retrieved cloud products. For simulation results, a cloudy pixel having a cloud  
457 liquid mass fraction larger than 0.5 is counted as a liquid pixel, otherwise, it is an ice  
458 pixel. Both CLAAS-2 and SEVIRI\_ML products and the corresponding retrievals  
459 derived from ICON simulations by the satellite forward operators (see section 2.4)  
460 provide binary cloud phase information (liquid or ice) only. For these data, the liquid  
461 cloud pixel number fraction is calculated as the ratio between the number of liquid  
462 cloud pixels and the sum of all cloudy pixels.

463

464 Liquid cloud pixel number fractions within clouds and at the cloud top are shown in  
465 Figure 8. Decrease in INP concentration has limited impacts on the liquid cloud pixel  
466 number fraction for in-cloud layers. Increase in INP concentration leads to a  
467 decrease in liquid cloud pixel number fraction but not monotonically (Figure 8a). The  
468 decrease in liquid cloud pixel number fraction is significant in the highest INP  
469 concentration case (case  $A \times 10^3$ ), while decreases in intermediate INP concentration  
470 cases (cases  $A \times 10^1$  and  $A \times 10^2$ ) are only obvious in temperature ranges from  $-30\text{ }^\circ\text{C}$   
471 to  $-20\text{ }^\circ\text{C}$  and from  $-15\text{ }^\circ\text{C}$  to  $-5\text{ }^\circ\text{C}$ . Switching off the rime-splintering process results  
472 in an increase in liquid cloud pixel number fraction in the temperature range between  
473  $-10\text{ }^\circ\text{C}$  and  $-3\text{ }^\circ\text{C}$ , which is consistent with the strong decrease in pixels of cloud  
474 liquid mass fraction lower than 0.9 in the same temperature range (Figure 7b). The  
475 temperature at which the liquid cloud pixel number fraction equals 0.5 is often  
476 termed “glaciation temperature”. The glaciation temperature shifts slightly to a  
477 warmer temperature by  $\sim 2\text{ }^\circ\text{C}$  at the highest INP concentration case (case  $A \times 10^3$ ,  
478 Figure 8a).

479

480 Sensitivities of the cloud phase to INP concentration are more complex at the cloud  
481 top than inside the cloud. Liquid cloud pixel number fractions at the cloud top  
482 calculated directly from ICON simulations on its native grid ( $\sim 1200\text{ m}$ ) are shown in  
483 Figure 8b. Cloud-top liquid pixel number fraction decreases significantly with  
484 increasing INP concentration. In the temperature range between  $-35\text{ }^\circ\text{C}$  and  $-15\text{ }^\circ\text{C}$ ,  
485 where heterogeneous freezing processes (immersion freezing and deposition  
486 nucleation) are dominant, the impact of INP is most pronounced. Above  $-15\text{ }^\circ\text{C}$ , the





487 impact of INP does not disappear, especially in the highest INP concentration case  
488 (case  $A \times 10^3$ ). This is mostly likely due to the sedimentation of ice crystals from upper  
489 layers and the secondary ice production invigorated by the Wegener-Bergeron-  
490 Findeisen process. Switching off the rime-splintering process increases cloud-top  
491 liquid pixel number fraction only slightly in the temperature range from  $-10\text{ }^\circ\text{C}$  to  $-$   
492  $3\text{ }^\circ\text{C}$  and is almost identical to the control run (case CTRL) outside this temperature  
493 range. Interestingly, the shift of glaciation temperature with increasing INP  
494 concentration is about  $8\text{ }^\circ\text{C}$  (Figure 8b) at the cloud top, which is stronger than that  
495 inside the clouds ( $\sim 2\text{ }^\circ\text{C}$ , Figure 8a). A possible explanation is that, typically, the  
496 vertical velocity at the cloud top is smaller than within the cloud and the ice formation  
497 through the Wegener-Bergeron-Findeisen process is expected to be more efficient.  
498 Thus, the Wegener-Bergeron-Findeisen process is more sensitive to INP perturbation  
499 at the cloud top than within clouds, and leads to the glaciation temperature shifting to  
500 be more significant at the cloud top.

501

502 Liquid cloud pixel number fractions at the cloud top calculated directly from ICON  
503 simulations on SEVIRI's grid ( $\sim 5000\text{ m}$ ) are shown in Figure 8c. They are noisier  
504 and do not exhibit the small minimum between  $-10\text{ }^\circ\text{C}$  and  $-3\text{ }^\circ\text{C}$  related to rime-  
505 splintering, but are otherwise very similar to Figure 8b. In contrast, the scale-aware  
506 and definition-aware ICON\_RTTOV\_CLAAS-2 cloud-top liquid pixel number fractions  
507 shown in Figure 8d differ markedly from the direct or regridded model output. Above  
508  $-23\text{ }^\circ\text{C}$ , increase and decrease in INP concentration both lead to a decrease in cloud-  
509 top liquid pixel number fraction at certain temperature, but the high INP  
510 concentration cases (cases  $A \times 10^2$  and  $A \times 10^3$ ), still exhibit the lowest liquid fractions,  
511 and case  $A \times 10^0_{\text{NSIP}}$  the highest. Thus, the fingerprints of primary and secondary  
512 ice formation are retained in the ICON\_RTTOV\_CLAAS-2 liquid fraction in this  
513 temperature range only for very strong perturbations. At the same time, it must be  
514 noted that the decrease of the liquid pixel number fraction to values around 0.8  
515 above  $-15\text{ }^\circ\text{C}$  is not related to the rime-splintering process, but to the application of  
516 the CLAAS-2 satellite simulator.

517

518 Below  $-23\text{ }^\circ\text{C}$ , in the high INP cases  $A \times 10^2$  and  $A \times 10^3$ , cloud-top liquid pixel number  
519 fractions even increase with increasing INP concentration. In moderate and low INP



520 cases, the impacts of INP perturbation are not pronounced. Moreover, the shape of  
521 cloud-top liquid pixel number fraction decreasing with cloud-top temperature is  
522 different from that in Figure 8b. Here, the fingerprints of the ice formation processes  
523 are completely lost. As demonstrated in Figure 8c, remapping of simulation data onto  
524 SEVIRI's coarser grid is not the cause of liquid pixel number fraction difference  
525 between direct ICON output and the ICON\_RTTOV\_CLAAS-2 diagnostics, but the  
526 loss of information through the postprocessing is responsible.

527

528 The satellite observed cloud-top liquid pixel number fraction from CLAAS-2 is plotted  
529 as a grey dashed line in Figure 8d. It does not reach 1.0 for all cases even as the  
530 cloud-top temperature is approaching 0 °C, and shows a different temperature  
531 dependency than the simulated curves. No matter how strong the INP concentration  
532 and rime-splintering are perturbed, the retrieved cloud-top liquid pixel number  
533 fractions from simulation data deviate strongly from the CLAAS-2 products. In this  
534 context one should note that in particular cloud edges have been found to be  
535 problematic situations for the cloud retrievals, being to some extent responsible for  
536 biasing the liquid-pixel fraction towards smaller values, in particular for the CLAAS-2  
537 data.

538

539 Finally, the comparison to observations is repeated with the SEVIRI\_ML retrieval  
540 scheme applied to both simulated radiances (ICON\_RTTOV\_SEVIRI\_ML) and the  
541 SEVIRI observations themselves (Figure 8e). As SEVIRI\_ML provides uncertainty  
542 estimates, pixels for which either the cloud mask uncertainty or the cloud phase  
543 uncertainty is larger than 10% are filtered out. While this ensures that only very  
544 certain values are kept, it has a significant impact on the number of remaining values  
545 as more than 90% of the pixels are filtered out. The resulting liquid pixel number  
546 fractions ICON\_RTTOV\_SEVIRI\_ML bear a much stronger similarity to the regridded  
547 model output in Figure 8c. Remaining differences are a noisier behavior, a plateau of  
548 non-zero liquid pixel number fractions even below -40 °C, and a general shift to  
549 lower temperatures. SEVIRI\_ML applied to observations (dashed black line in Figure  
550 8e), with the same uncertainty criterion, exhibits the expected behavior with a liquid  
551 fraction of approximately 1 above -10 and 0 °C below approximately -30 °C, and  
552 results in a very good agreement to the  $A \times 10^3$  case.



553 **3.5. Sensitivity of cloud phase to atmospheric stability perturbations**

554 In addition to the reference run (case CTRL), four cases with perturbations in initial  
555 temperatures are analyzed. Mean updraft velocities increase gradually from the low  
556 CAPE case INC05 to high CAPE case DEC05 (Figure 9) and cause differences in  
557 cloud microphysics and cloud phase distributions.

558

559 In-cloud and cloud-top liquid cloud pixel number fractions for the five cases are  
560 shown in Figure 10. Systematic shifting of liquid cloud pixel number fractions is  
561 detected both inside clouds and at the cloud top. Liquid cloud pixel number fraction  
562 decreases with increasing CAPE from INC05 to DEC05. Both in-cloud and cloud-top  
563 glaciation temperatures shift toward warmer temperatures as the CAPE increasing  
564 from case INC05 to DEC05. This is different from the results reported by [Hoose et al.](#)  
565 [\(2018\)](#) that cloud-top glaciation temperatures hardly changed with increasing  
566 temperature in the boundary-layer by 2 °C, and appears to be contradictory to the  
567 expectation that stronger vertical velocities result in a lower glaciation temperature  
568 due to suppression of the Wegener-Bergeron-Findeisen process ([Korolev, 2007](#)).  
569 Further analysis (not shown) revealed that the mass concentration of cloud ice  
570 particle increases while the mass concentration of cloud droplet decreases with the  
571 increase in CAPE from case INC05 to DEC05. Moreover, homogeneous and  
572 heterogeneous freezing are both enhanced in the high CAPE cases (Figure 11),  
573 possibly due to more transport of moisture to upper levels in the stronger updrafts  
574 (Figure 9). With more ice generated, the Wegener-Begeron-Findeisen process can  
575 be stimulated despite the higher updrafts. Interestingly, cloud-top liquid pixel number  
576 fractions from the two high CAPE cases (cases DEC03 and DEC05) are closer to  
577 SEVIRI observations, both using the CLAAS-2 retrieval (Figure 10c) and the  
578 SEVIRI\_ML retrieval (Figure 10d), especially in the temperature range between -10  
579 and -28 °C. Overall, perturbing initial thermodynamic states or CAPE of convective  
580 clouds is as important as the modifications to cloud heterogeneous freezing  
581 parameterizations.

582 **4. Conclusions**

583 Remote sensing products, which cover the entire globe, provide a unique opportunity  
584 to constrain the representation of cloud microphysics in global and regional



585 numerical models. In this study, instead of comparing simulation results to satellite  
586 observations directly, we derived cloud properties using a radiative transfer model  
587 and two different satellite remote sensing retrieval algorithms and then performed the  
588 comparison. This enables us to evaluate cloud microphysical processes of numerical  
589 models using satellite observations directly. A series of numerical experiments were  
590 performed applying convection-permitting simulations with perturbations in INP  
591 concentrations and initial thermodynamic states to investigate their impacts on cloud  
592 phase distributions in deep convective clouds. Simulation results were compared to  
593 cloud properties derived from SEVIRI measurements to evaluate the model  
594 performance in simulating cloud-top microphysical properties.

595

596 INP concentration was found to have a significant role in shaping cloud phase  
597 distributions both within clouds and at the cloud top. Cloud liquid pixel number  
598 fraction decreases with increasing INP concentration both within the cloud and at the  
599 cloud top, indicating a higher glaciation temperature and more intense  
600 heterogeneous freezing processes in enhanced INP concentration cases.

601 Interestingly, the influences of INP do not increase linearly but are more pronounced  
602 in the high INP concentration cases. In addition, the shifting of glaciation temperature  
603 is more significant at the cloud top than within the cloud, which means the impact of  
604 INP concentration on cloud phase distribution is more pronounced at the cloud top.  
605 This has implications for analyzing cloud products retrieved from passive remote  
606 sensing observations. It turned out that with the CLAAS-2 retrieval scheme, the INP  
607 sensitivity of the cloud-top phase distribution was not detectable, while the  
608 SEVIRI\_ML retrieval scheme, for which the most uncertain pixels could be excluded,  
609 resulted in a better agreement and retained the sensitivity to INP. In contrast,  
610 secondary ice production via rime-splintering did not have a detectable impact on the  
611 cloud-top phase distribution. Therefore, in future studies, we recommend using the  
612 SEVIRI\_ML retrieval scheme and SEVIRI\_ML satellite-based cloud products.

613

614 Total cloud ice mass concentrations do not increase but decrease with increasing  
615 INP concentrations in the simulated deep convective clouds. Process rate analyses  
616 reveal that heterogeneous freezing process rates increase with increasing INP  
617 concentrations, while homogeneous freezing process rates decrease with increasing  
618 INP concerns. The competition between heterogeneous freezing and homogeneous



619 freezing for water vapor suppresses ice formation via homogeneous freezing, which  
620 is the dominant nucleation process in the simulated deep convective clouds, and  
621 hence decreases the cloud ice mass concentration. The increase in heterogeneous  
622 nucleation in high INP cases invigorates riming and collection processes of ice  
623 particles, making it easier for small ice crystals to grow into large ice aggregates and  
624 sediment to lower levels. This is the reason why precipitation increases in enhanced  
625 INP cases.

626

627 Perturbations in initial thermodynamic states have a strong impact on the cloud  
628 phase distribution both within the cloud and at the cloud top, although the used  
629 perturbations might be rather large compared to initial condition uncertainty in a  
630 weather forecasting context. To completely distinguish microphysical impacts from  
631 thermodynamic impacts, applying a piggybacking approach ([Grabowski, 2015](#);  
632 [Thomas et al., 2023](#)) in future simulations is necessary.

633

634 Utilizing satellite forward operator (the RTTOV radiative model) and remote sensing  
635 retrieval algorithms enable us to derive cloud-top microphysical products and  
636 compare simulation results to satellite products more consistently. However, there  
637 are significant differences in retrieved cloud-top liquid fractions between model  
638 simulations and satellite products. The sources of errors are very complicated and  
639 may come from simulation results, satellite operators, or retrieval algorithms, which  
640 will be investigated in the future. Moreover, the cloud-top property analysis  
641 presented in this study is based on domain-wide statistics, including clouds of  
642 varying types. Statistical results could differ if individual clouds are tracked, as clouds  
643 differ in different experiments in terms of locations and extensions. Although there  
644 are significant uncertainties in satellite forward operators and retrieval algorithms,  
645 passively remote-sensed cloud products provide potential opportunities to constrain  
646 microphysical processes in numerical models.

647

648 Simulation results of this study reveal a close dependence of heterogeneous  
649 freezing and cloud phase distribution on INP concentrations. Despite this finding, the  
650 ice formation processes in deep convective clouds remain poorly understood. It is  
651 necessary to investigate how and in which conditions the competition of  
652 heterogeneous with homogeneous freezing for water vapor and cloud water depends



653 on INP availability and vertical velocities in different types of deep convective clouds.  
654 Moreover, the importance of other secondary ice production processes than rime-  
655 splintering (droplet shattering and collisional breakup) in deep convective clouds  
656 need to be quantified in the future.

657

### 658 **Competing interests**

659 One of the (co-)authors (Corinna Hoose) is a member of the editorial board of  
660 Atmospheric Chemistry and Physics.

661

### 662 **Acknowledgments**

663 This project has received funding from the European Research Council (ERC) under  
664 the European Union's Horizon 2020 research and innovation programme under grant  
665 agreement 714062 (ERC Starting Grant "C2Phase"). We gratefully acknowledge the  
666 computing time allowed by the German Climate Computing Centre (DKRZ) on the  
667 HPC system Mistral and the Steinbuch Centre for Computing (SCC) on the HPC  
668 system ForHLR II. The contribution of Martin Stengel was supported by EUMETSAT  
669 and its member states through CM SAF.

670

### 671 **References**

- 672 Barrett, A. I. and Hoose, C.: Microphysical pathways active within thunderstorms and  
673 their sensitivity to CCN concentration and wind shear, *Journal of Geophysical*  
674 *Research: Atmospheres*, 128, e2022JD036965,  
675 <https://doi.org/10.1029/2022JD036965>, 2023.
- 676 Barthlott, C. and Hoose, C.: Aerosol effects on clouds and precipitation over central  
677 Europe in different weather regimes, *Journal of the Atmospheric Sciences*, 75,  
678 4247-4264, <https://doi.org/10.1175/JAS-D-18-0110.1>, 2018.
- 679 Benas, N., Finkensieper, S., Stengel, M., van Zadelhoff, G. J., Hanschmann, T.,  
680 Hollmann, R., and Meirink, J. F.: The MSG-SEVIRI-based cloud property data  
681 record CLAAS-2, *Earth Syst. Sci. Data*, 9, 415-434,  
682 <http://dx.doi.org/10.5194/essd-9-415-2017>, 2017.
- 683 Bruno, O., Hoose, C., Storelvmo, T., Coopman, Q., and Stengel, M.: Exploring the  
684 cloud top phase partitioning in different cloud types using active and passive  
685 satellite sensors, *Geophysical Research Letters*, 48, e2020GL089863-  
686 e082020GL089863, <https://doi.org/10.1029/2020GL089863>, 2021.



- 687 Coopman, Q., Hoose, C., and Stengel, M.: Analysis of the thermodynamic phase  
688 transition of tracked convective clouds based on geostationary satellite  
689 observations, *Journal of Geophysical Research: Atmospheres*, 125,  
690 e2019JD032146, <https://doi.org/10.1029/2019JD032146>, 2020.
- 691 Coopman, Q., Hoose, C., and Stengel, M.: Analyzing the thermodynamic phase  
692 partitioning of mixed phase clouds over the southern ocean using passive  
693 satellite observations, *Geophysical Research Letters*, 48, e2021GL093225,  
694 <https://doi.org/10.1029/2021GL093225>, 2021.
- 695 Dee, D. P., Uppala, S. M., Simmons, A. J., Berrisford, P., Poli, P., Kobayashi, S.,  
696 Andrae, U., Balmaseda, M. A., Balsamo, G., Bauer, P., Bechtold, P., Beljaars,  
697 A. C. M., van de Berg, L., Bidlot, J., Bormann, N., Delsol, C., Dragani, R.,  
698 Fuentes, M., Geer, A. J., Haimberger, L., Healy, S. B., Hersbach, H., Hólm, E.  
699 V., Isaksen, I., Kållberg, P., Köhler, M., Matricardi, M., McNally, A. P., Monge-  
700 Sanz, B. M., Morcrette, J. J., Park, B. K., Peubey, C., de Rosnay, P.,  
701 Tavolato, C., Thépaut, J. N., and Vitart, F.: The ERA-Interim reanalysis:  
702 configuration and performance of the data assimilation system, *Quarterly  
703 Journal of the Royal Meteorological Society*, 137, 553-597,  
704 <https://doi.org/10.1002/qj.828>, 2011.
- 705 Deng, X., Xue, H., and Meng, Z.: The effect of ice nuclei on a deep convective cloud  
706 in South China, *Atmospheric Research*, 206, 1-12,  
707 <https://doi.org/10.1016/j.atmosres.2018.02.013>, 2018.
- 708 Derrien, M. and Le Gléau, H.: MSG/SEVIRI cloud mask and type from SAFNWC,  
709 *International Journal of Remote Sensing*, 26, 4707-4732,  
710 <https://doi.org/10.1080/01431160500166128>, 2005.
- 711 Fan, J., Comstock, J. M., and Ovchinnikov, M.: The cloud condensation nuclei and  
712 ice nuclei effects on tropical anvil characteristics and water vapor of the  
713 tropical tropopause layer, *Environmental Research Letters*, 5, 044005,  
714 <https://doi.org/10.1088/1748-9326/5/4/044005>, 2010.
- 715 Fan, J., Wang, Y., Rosenfeld, D., and Liu, X.: Review of aerosol–cloud interactions:  
716 Mechanisms, significance, and challenges, *Journal of the Atmospheric  
717 Sciences*, 73, 4221-4252, <https://doi.org/10.1175/JAS-D-16-0037.1>, 2016.
- 718 Field, P. R., Hogan, R. J., Brown, P. R. A., Illingworth, A. J., Choulaton, T. W., Kaye,  
719 P. H., Hirst, E., and Greenaway, R.: Simultaneous radar and aircraft  
720 observations of mixed-phase cloud at the 100 m scale, *Quarterly Journal of  
721 the Royal Meteorological Society*, 130, 1877-1904,  
722 <https://doi.org/10.1256/qj.03.102>, 2004.
- 723 Gassmann, A. and Herzog, H.-J.: Towards a consistent numerical compressible non-  
724 hydrostatic model using generalized Hamiltonian tools, *Quarterly Journal of  
725 the Royal Meteorological Society*, 134, 1597-1613,  
726 <http://dx.doi.org/10.1002/qj.297>, 2008.
- 727 Geiss, S., Scheck, L., de Lozar, A., and Weissmann, M.: Understanding the model  
728 representation of clouds based on visible and infrared satellite observations,  
729 *Atmos. Chem. Phys.*, 21, 12273-12290, [https://doi.org/10.5194/acp-21-12273-  
730 2021](https://doi.org/10.5194/acp-21-12273-2021), 2021.
- 731 Grabowski, W. W.: Untangling microphysical impacts on deep convection applying a  
732 novel modeling methodology, *Journal of the Atmospheric Sciences*, 72, 2446-  
733 2464, <https://doi.org/10.1175/JAS-D-14-0307.1>, 2015.
- 734 Grabowski, W. W., Morrison, H., Shima, S.-I., Abade, G. C., Dziekan, P., and  
735 Pawlowska, H.: Modeling of cloud microphysics: Can we do better?, *Bulletin*



- 736 of the American Meteorological Society, 100, 655-672,  
737 <https://doi.org/10.1175/BAMS-D-18-0005.1>, 2019.
- 738 Hande, L. B., Engler, C., Hoose, C., and Tegen, I.: Seasonal variability of Saharan  
739 desert dust and ice nucleating particles over Europe, *Atmos. Chem. Phys.*,  
740 15, 4389-4397, <http://dx.doi.org/10.5194/acp-15-4389-2015>, 2015.
- 741 Hande, L. B., Engler, C., Hoose, C., and Tegen, I.: Parameterizing cloud  
742 condensation nuclei concentrations during HOPE, *Atmos. Chem. Phys.*, 16,  
743 12059-12079, <http://dx.doi.org/10.5194/acp-16-12059-2016>, 2016.
- 744 Hawker, R. E., Miltenberger, A. K., Wilkinson, J. M., Hill, A. A., Shipway, B. J., Cui,  
745 Z., Cotton, R. J., Carslaw, K. S., Field, P. R., and Murray, B. J.: The  
746 temperature dependence of ice-nucleating particle concentrations affects the  
747 radiative properties of tropical convective cloud systems, *Atmos. Chem.*  
748 *Phys.*, 21, 5439-5461, <https://doi.org/10.5194/acp-21-5439-2021>, 2021.
- 749 Heymsfield, A. J., Miloshevich, L. M., Schmitt, C., Bansemer, A., Twohy, C., Poellot,  
750 M. R., Fridlind, A., and Gerber, H.: Homogeneous ice nucleation in subtropical  
751 and tropical convection and its influence on cirrus anvil microphysics, *Journal*  
752 *of the Atmospheric Sciences*, 62, 41-64, <http://dx.doi.org/10.1175/JAS-3360.1>,  
753 2005.
- 754 Hoose, C. and Möhler, O.: Heterogeneous ice nucleation on atmospheric aerosols: a  
755 review of results from laboratory experiments, *Atmos. Chem. Phys.*, 12, 9817-  
756 9854, <https://doi.org/10.5194/acp-12-9817-2012>, 2012.
- 757 Hoose, C., Karrer, M., and Barthlott, C.: Cloud top phase distributions of simulated  
758 deep convective clouds, *Journal of Geophysical Research: Atmospheres*,  
759 123, 10,410-464,476, <https://doi.org/10.1029/2018JD028381>, 2018.
- 760 Kanji, Z. A., Ladino, L. A., Wex, H., Boose, Y., Burkert-Kohn, M., Cziczo, D. J., and  
761 Krämer, M.: Overview of ice nucleating particles, *Meteorological Monographs*,  
762 58, 1.1-1.33, <https://doi.org/10.1175/AMSMONOGRAPHS-D-16-0006.1>, 2017.
- 763 Kärcher, B., Hendricks, J., and Lohmann, U.: Physically based parameterization of  
764 cirrus cloud formation for use in global atmospheric models, *Journal of*  
765 *Geophysical Research: Atmospheres*, 111,  
766 <https://doi.org/10.1029/2005JD006219>, 2006.
- 767 Kay, J. E., L'Ecuyer, T., Pendergrass, A., Chepfer, H., Guzman, R., and Yettella, V.:  
768 Scale-aware and definition-aware evaluation of modeled near-surface  
769 precipitation frequency using CloudSat observations, *Journal of Geophysical*  
770 *Research: Atmospheres*, 123, 4294-4309,  
771 <https://doi.org/10.1002/2017JD028213>, 2018.
- 772 Keil, C., Baur, F., Bachmann, K., Rasp, S., Schneider, L., and Barthlott, C.: Relative  
773 contribution of soil moisture, boundary-layer and microphysical perturbations  
774 on convective predictability in different weather regimes, *Quarterly Journal of*  
775 *the Royal Meteorological Society*, 145, 3102-3115,  
776 <https://doi.org/10.1002/qj.3607>, 2019.
- 777 Korolev, A. and Isaac, G. A.: Relative humidity in liquid, mixed-phase, and ice  
778 clouds, *Journal of the Atmospheric Sciences*, 63, 2865-2880,  
779 <https://doi.org/10.1175/JAS3784.1>, 2006.
- 780 Korolev, A.: Limitations of the Wegener–Bergeron–Findeisen mechanism in the  
781 evolution of mixed-phase clouds, *Journal of the Atmospheric Sciences*, 64,  
782 3372-3375, <http://dx.doi.org/10.1175/JAS4035.1>, 2007.
- 783 Korolev, A., McFarquhar, G., Field, P. R., Franklin, C., Lawson, P., Wang, Z.,  
784 Williams, E., Abel, S. J., Axisa, D., Borrmann, S., Crosier, J., Fugal, J.,  
785 Krämer, M., Lohmann, U., Schlenczek, O., Schnaiter, M., and Wendisch, M.:





- 786 Mixed-phase clouds: Progress and challenges, *Meteorological Monographs*,  
787 58, 5.1-5.50, <https://doi.org/10.1175/AMSMONOGRAPHS-D-17-0001.1>, 2017.
- 788 Korolev, A. V., Isaac, G. A., Cober, S. G., Strapp, J. W., and Hallett, J.:  
789 Microphysical characterization of mixed-phase clouds, *Quarterly Journal of*  
790 *the Royal Meteorological Society*, 129, 39-65,  
791 <https://doi.org/10.1256/qj.01.204>, 2003.
- 792 Li, R. and Min, Q. L.: Impacts of mineral dust on the vertical structure of precipitation,  
793 *Journal of Geophysical Research: Atmospheres*, 115,  
794 <https://doi.org/10.1029/2009JD011925>, 2010.
- 795 Lohmann, U. and Hoose, C.: Sensitivity studies of different aerosol indirect effects in  
796 mixed-phase clouds, *Atmos. Chem. Phys.*, 9, 8917-8934,  
797 <https://doi.org/10.5194/acp-9-8917-2009>, 2009.
- 798 Matus, A. V. and L'Ecuyer, T. S.: The role of cloud phase in Earth's radiation budget,  
799 *Journal of Geophysical Research: Atmospheres*, 122, 2559-2578,  
800 <https://doi.org/10.1002/2016JD025951>, 2017.
- 801 McCoy, D. T., Tan, I., Hartmann, D. L., Zelinka, M. D., and Storelvmo, T.: On the  
802 relationships among cloud cover, mixed-phase partitioning, and planetary  
803 albedo in GCMs, *Journal of Advances in Modeling Earth Systems*, 8, 650-668,  
804 <https://doi.org/10.1002/2015MS000589>, 2016.
- 805 Menzel, W. P., Smith, W. L., and Stewart, T. R.: Improved cloud motion wind vector  
806 and altitude assignment using VAS, *Journal of Applied Meteorology and*  
807 *Climatology*, 22, 377-384, [https://doi.org/10.1175/1520-0450\(1983\)022<0377:ICMWVA>2.0.CO;2](https://doi.org/10.1175/1520-0450(1983)022<0377:ICMWVA>2.0.CO;2), 1983.
- 808 Miltenberger, A. K. and Field, P. R.: Sensitivity of mixed-phase moderately deep  
809 convective clouds to parameterizations of ice formation – an ensemble  
810 perspective, *Atmos. Chem. Phys.*, 21, 3627-3642,  
811 <http://dx.doi.org/10.5194/acp-21-3627-2021>, 2021.
- 812  
813 Min, Q. L., Li, R., Lin, B., Joseph, E., Wang, S., Hu, Y., Morris, V., and Chang, F.:  
814 Evidence of mineral dust altering cloud microphysics and precipitation,  
815 *Atmospheric Chemistry and Physics*, 9, 3223-3231,  
816 <https://doi.org/10.5194/acp-9-3223-2009>, 2009.
- 817 Nakajima, T. and King, M. D.: Determination of the optical thickness and effective  
818 particle radius of clouds from reflected solar radiation measurements. Part I:  
819 Theory, *Journal of Atmospheric Sciences*, 47, 1878-1893,  
820 [https://doi.org/10.1175/1520-0469\(1990\)047<1878:DOTOTA>2.0.CO;2](https://doi.org/10.1175/1520-0469(1990)047<1878:DOTOTA>2.0.CO;2), 1990.
- 821 Noh, Y.-J., Seaman, C. J., Vonder Haar, T. H., and Liu, G.: In situ aircraft  
822 measurements of the vertical distribution of liquid and ice water content in  
823 midlatitude mixed-phase clouds, *Journal of Applied Meteorology and*  
824 *Climatology*, 52, 269-279, <https://doi.org/10.1175/JAMC-D-11-0202.1>, 2013.
- 825 Pavolonis, M. J., Heidinger, A. K., and Uttal, T.: Daytime global cloud typing from  
826 AVHRR and VIIRS: Algorithm description, validation, and comparisons,  
827 *Journal of Applied Meteorology*, 44, 804-826,  
828 <https://doi.org/10.1175/JAM2236.1>, 2005.
- 829 Pinto, J. O.: Autumnal mixed-phase cloudy boundary layers in the Arctic, *Journal of*  
830 *the Atmospheric Sciences*, 55, 2016-2038, [https://doi.org/10.1175/1520-0469\(1998\)055<2016:AMPCBL>2.0.CO;2](https://doi.org/10.1175/1520-0469(1998)055<2016:AMPCBL>2.0.CO;2), 1998.
- 831  
832 Pscheidt, I., Senf, F., Heinze, R., Deneke, H., Trömel, S., and Hohenegger, C.: How  
833 organized is deep convection over Germany?, *Quarterly Journal of the Royal*  
834 *Meteorological Society*, 145, 2366-2384, <http://dx.doi.org/10.1002/qj.3552>,  
835 2019.



- 836 Roebeling, R. A., Feijt, A. J., and Stammes, P.: Cloud property retrievals for climate  
837 monitoring: Implications of differences between Spinning Enhanced Visible  
838 and Infrared Imager (SEVIRI) on METEOSAT-8 and Advanced Very High  
839 Resolution Radiometer (AVHRR) on NOAA-17, *Journal of Geophysical*  
840 *Research: Atmospheres*, 111, <https://doi.org/10.1029/2005JD006990>, 2006.
- 841 Rosenfeld, D. and Woodley, W. L.: Deep convective clouds with sustained  
842 supercooled liquid water down to -37.5 °C, *Nature*, 405, 440-442,  
843 <https://doi.org/10.1038/35013030>, 2000.
- 844 Rosenfeld, D., Yu, X., Liu, G., Xu, X., Zhu, Y., Yue, Z., Dai, J., Dong, Z., Dong, Y.,  
845 and Peng, Y.: Glaciation temperatures of convective clouds ingesting desert  
846 dust, air pollution and smoke from forest fires, *Geophysical Research Letters*,  
847 38, <https://doi.org/10.1029/2011GL049423>, 2011.
- 848 Rybka, H., Burkhardt, U., Köhler, M., Arka, I., Bugliaro, L., Görsdorf, U., Horváth, Á.,  
849 Meyer, C. I., Reichardt, J., Seifert, A., and Strandgren, J.: The behavior of  
850 high-CAPE (convective available potential energy) summer convection in  
851 large-domain large-eddy simulations with ICON, *Atmos. Chem. Phys.*, 21,  
852 4285-4318, <http://dx.doi.org/10.5194/acp-21-4285-2021>, 2021.
- 853 Saunders, R., Hocking, J., Turner, E., Rayer, P., Rundle, D., Brunel, P., Vidot, J.,  
854 Roquet, P., Matricardi, M., Geer, A., Bormann, N., and Lupu, C.: An update on  
855 the RTTOV fast radiative transfer model (currently at version 12), *Geosci.*  
856 *Model Dev.*, 11, 2717-2737, <http://dx.doi.org/10.5194/gmd-11-2717-2018>,  
857 2018.
- 858 Schmetz, J., Holmlund, K., Hoffman, J., Strauss, B., Mason, B., Gaertner, V., Koch,  
859 A., and Van De Berg, L.: Operational cloud-motion winds from meteosat  
860 infrared images, *Journal of Applied Meteorology and Climatology*, 32, 1206-  
861 1225, [https://doi.org/10.1175/1520-  
862 0450\(1993\)032<1206:OCMWFM>2.0.CO;2](https://doi.org/10.1175/1520-0450(1993)032<1206:OCMWFM>2.0.CO;2), 1993.
- 863 Schmetz, J., Pili, P., Tjemkes, S., Just, D., Kerkmann, J., Rota, S., and Ratier, A.: An  
864 introduction to meteosat second generation (MSG), *Bulletin of the American*  
865 *Meteorological Society*, 83, 977-992, [http://dx.doi.org/10.1175/1520-  
866 0477\(2002\)083<0977:AITMSG>2.3.CO;2](http://dx.doi.org/10.1175/1520-0477(2002)083<0977:AITMSG>2.3.CO;2), 2002.
- 867 Seifert, A. and Beheng, K. D.: A two-moment cloud microphysics parameterization  
868 for mixed-phase clouds. Part 1: Model description, *Meteorology and*  
869 *Atmospheric Physics*, 92, 45-66, [http://dx.doi.org/10.1007/s00703-005-0112-  
870 4](http://dx.doi.org/10.1007/s00703-005-0112-4), 2006.
- 871 Senf, F., Voigt, A., Clerbaux, N., Hünerbein, A., and Deneke, H.: Increasing  
872 resolution and resolving convection improve the simulation of cloud-radiative  
873 effects over the North Atlantic, *Journal of Geophysical Research:*  
874 *Atmospheres*, 125, e2020JD032667, <https://doi.org/10.1029/2020JD032667>,  
875 2020.
- 876 Stengel, M., Kniffka, A., Meirink, J. F., Lockhoff, M., Tan, J., and Hollmann, R.:  
877 CLAAS: the CM SAF cloud property data set using SEVIRI, *Atmos. Chem.*  
878 *Phys.*, 14, 4297-4311, <http://dx.doi.org/10.5194/acp-14-4297-2014>, 2014.
- 879 Stengel, M., Stapelberg, S., Sus, O., Finkensieper, S., Würzler, B., Philipp, D.,  
880 Hollmann, R., Poulsen, C., Christensen, M., and McGarragh, G.: Cloud\_cci  
881 Advanced Very High Resolution Radiometer post meridiem (AVHRR-PM)  
882 dataset version 3: 35-year climatology of global cloud and radiation  
883 properties, *Earth Syst. Sci. Data*, 12, 41-60, 10.5194/essd-12-41-2020, 2020.



- 884 Stephens, G. L.: Radiation profiles in extended water clouds. II: Parameterization  
885 schemes, *Journal of Atmospheric Sciences*, 35, 2123-2132,  
886 [https://doi.org/10.1175/1520-0469\(1978\)035<2123:RPIEWC>2.0.CO;2](https://doi.org/10.1175/1520-0469(1978)035<2123:RPIEWC>2.0.CO;2), 1978.
- 887 Stith, J. L., Haggerty, J. A., Heymsfield, A., and Grainger, C. A.: Microphysical  
888 characteristics of tropical updrafts in clean conditions, *Journal of Applied*  
889 *Meteorology*, 43, 779-794, <https://doi.org/10.1175/2104.1>, 2004.
- 890 Takeishi, A. and Storelvmo, T.: A study of enhanced heterogeneous ice nucleation in  
891 simulated deep convective clouds observed during DC3, *Journal of*  
892 *Geophysical Research: Atmospheres*, 123, 3396-3420,  
893 <https://doi.org/10.1029/2018JD028889>, 2018.
- 894 Taylor, J. W., Choulaton, T. W., Blyth, A. M., Liu, Z., Bower, K. N., Crosier, J.,  
895 Gallagher, M. W., Williams, P. I., Dorsey, J. R., Flynn, M. J., Bennett, L. J.,  
896 Huang, Y., French, J., Korolev, A., and Brown, P. R. A.: Observations of cloud  
897 microphysics and ice formation during COPE, *Atmos. Chem. Phys.*, 16, 799-  
898 826, <https://doi.org/10.5194/acp-16-799-2016>, 2016.
- 899 Thomas, J., Barrett, A., and Hoose, C.: Temperature and cloud condensation nuclei  
900 (CCN) sensitivity of orographic precipitation enhanced by a mixed-phase  
901 seeder–feeder mechanism: a case study for the 2015 Cumbria flood, *Atmos.*  
902 *Chem. Phys.*, 23, 1987-2002, [10.5194/acp-23-1987-2023](https://doi.org/10.5194/acp-23-1987-2023), 2023.
- 903 Twohy, C. H.: Measurements of Saharan dust in convective clouds over the tropical  
904 eastern Atlantic ocean, *Journal of the Atmospheric Sciences*, 72, 75-81,  
905 <https://doi.org/10.1175/JAS-D-14-0133.1>, 2015.
- 906 van den Heever, S. C., Carrió, G. G., Cotton, W. R., DeMott, P. J., and Prenni, A. J.:  
907 Impacts of nucleating aerosol on Florida storms. Part I: Mesoscale  
908 simulations, *Journal of the Atmospheric Sciences*, 63, 1752-1775,  
909 <https://doi.org/10.1175/JAS3713.1>, 2006.
- 910 Vignon, É., Alexander, S. P., DeMott, P. J., Sotiropoulou, G., Gerber, F., Hill, T. C.  
911 J., Marchand, R., Nenes, A., and Berne, A.: Challenging and improving the  
912 simulation of mid-level mixed-phase clouds over the high-latitude southern  
913 ocean, *Journal of Geophysical Research: Atmospheres*, 126,  
914 e2020JD033490, <https://doi.org/10.1029/2020JD033490>, 2021.
- 915 Wan, H., Giorgetta, M. A., Zängl, G., Restelli, M., Majewski, D., Bonaventura, L.,  
916 Fröhlich, K., Reinert, D., Rípodas, P., Kornblueh, L., and Förstner, J.: The  
917 ICON-1.2 hydrostatic atmospheric dynamical core on triangular grids – Part 1:  
918 Formulation and performance of the baseline version, *Geosci. Model Dev.*, 6,  
919 735-763, <http://dx.doi.org/10.5194/gmd-6-735-2013>, 2013.
- 920 Zängl, G., Reinert, D., Rípodas, P., and Baldauf, M.: The ICON (ICOsahedral Non-  
921 hydrostatic) modelling framework of DWD and MPI-M: Description of the non-  
922 hydrostatic dynamical core, *Quarterly Journal of the Royal Meteorological*  
923 *Society*, 141, 563-579, <http://dx.doi.org/10.1002/qj.2378>, 2015.
- 924 Zhao, B., Wang, Y., Gu, Y., Liou, K.-N., Jiang, J. H., Fan, J., Liu, X., Huang, L., and  
925 Yung, Y. L.: Ice nucleation by aerosols from anthropogenic pollution, *Nature*  
926 *Geoscience*, 12, 602-607, [10.1038/s41561-019-0389-4](https://doi.org/10.1038/s41561-019-0389-4), 2019.
- 927 Zhao, X., Liu, X., Burrows, S. M., and Shi, Y.: Effects of marine organic aerosols as  
928 sources of immersion-mode ice-nucleating particles on high-latitude mixed-  
929 phase clouds, *Atmos. Chem. Phys.*, 21, 2305-2327,  
930 <https://doi.org/10.5194/acp-21-2305-2021>, 2021.
- 931



932 **Tables:**

933

934 Table 1: Setups of simulations performed in this study.

Num	Experiment	Description
1	$A \times 10^0$ (CTRL)	Without any perturbations, the CTRL run, used as a reference.
2	$A \times 10^{-2}$	INP concentrations for both immersion and deposition mode are scaled by multiplying parameter A in Equation (1) by $10^{-2}$ .
3	$A \times 10^{-1}$	Same as num. 2, but multiplying by $10^{-1}$ .
4	$A \times 10^1$	Same as num. 2, but multiplying by $10^1$ .
5	$A \times 10^2$	Same as num. 2, but multiplying by $10^2$ .
6	$A \times 10^3$	Same as num. 2, but multiplying by $10^3$ .
7	$A \times 10^0$ _NSIP	INP concentration as in CTRL. The secondary ice production (rime-splintering process) is switched off.
8	DEC05	Initial and lateral temperature decreases from 3 to 12 km with a maximum increment of 5 K. No perturbations in INPs ( $A \times 10^0$ ).
9	DEC03	Same as num. 8, but with a maximum increment of 3 K.
10	INC03	Initial and lateral temperature increases from 3 to 12 km with a maximum increment of 3 K. No perturbations in INPs ( $A \times 10^0$ ).
11	INC05	Same as num. 10, but with a maximum increment of 5 K.

935

936

937

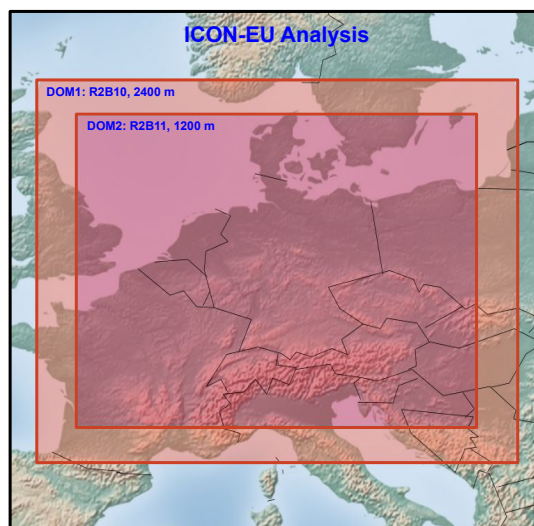
938



939 **Figures:**

940

941



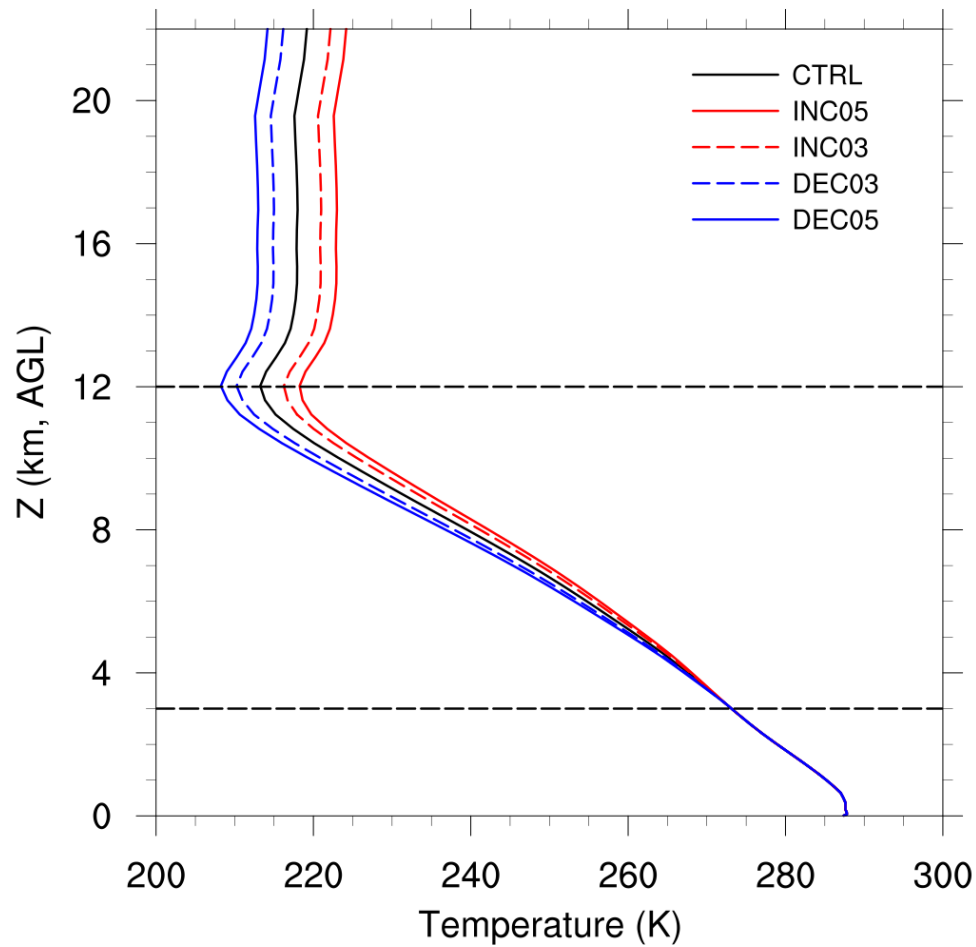
942

943 Figure 1: The simulation domains.

944



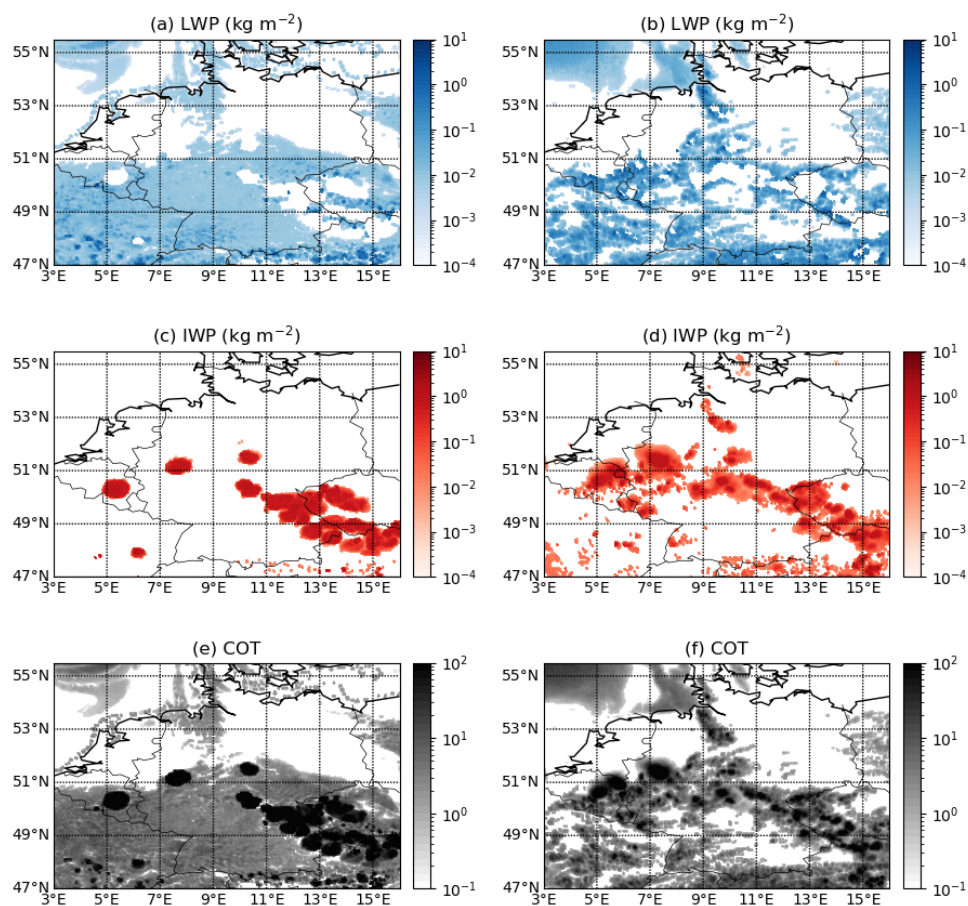
945



946

947 Figure 2: Domain averaged initial temperature profiles. The same modification was  
948 applied to the lateral boundary conditions.

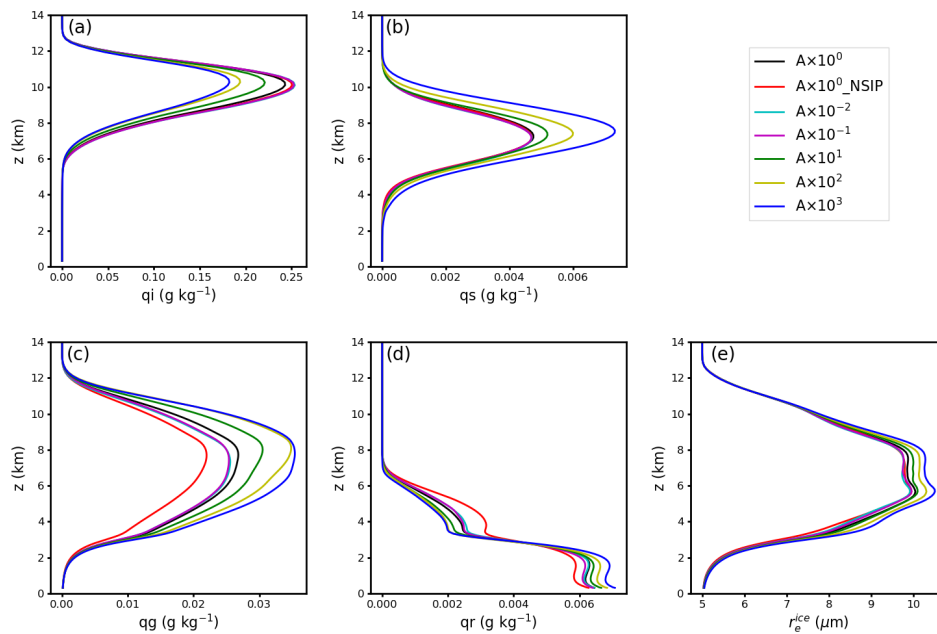
949



950

951 Figure 3: Spatial distributions of retrieved cloud liquid water path (LWP), ice water  
952 path (IWP), and cloud optical thickness (COT) at 13:00 UTC. The left panel is for the  
953 CTRL case (a, c, e) and the right panel is for the CLAAS-2 product (b, d, f).

954

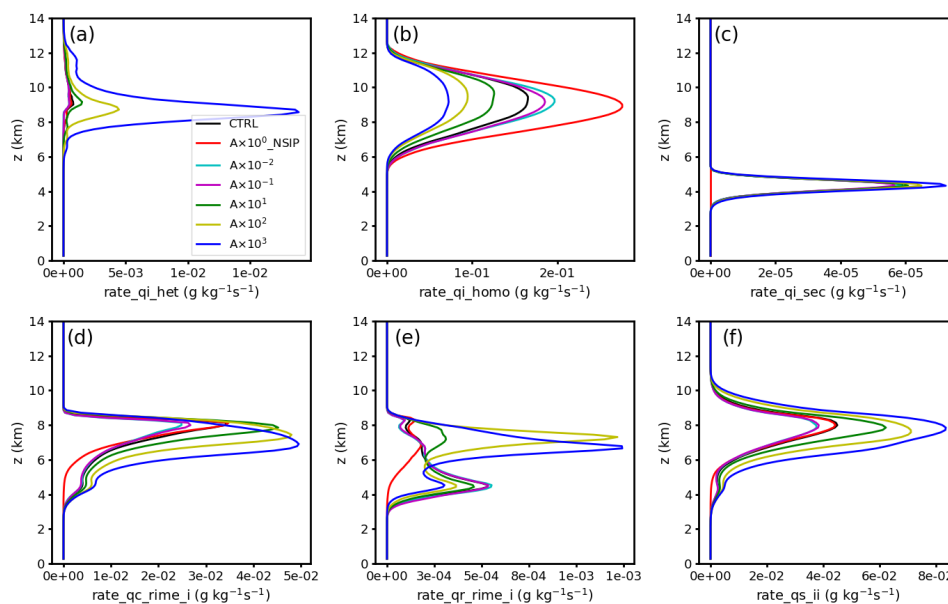


955

956 Figure 4: Spatial- and time-averaged (9:00~19:00) profiles of cloud mass mixing  
957 ratios of (a) ice crystals, (b) snow, (c) graupel, (d) rainwater, and (e) ice crystal  
958 effective radius. Mass mixing ratio unit is  $\text{g kg}^{-1}$  and the unit of ice crystal effective  
959 radius is  $\mu\text{m}$ .

960

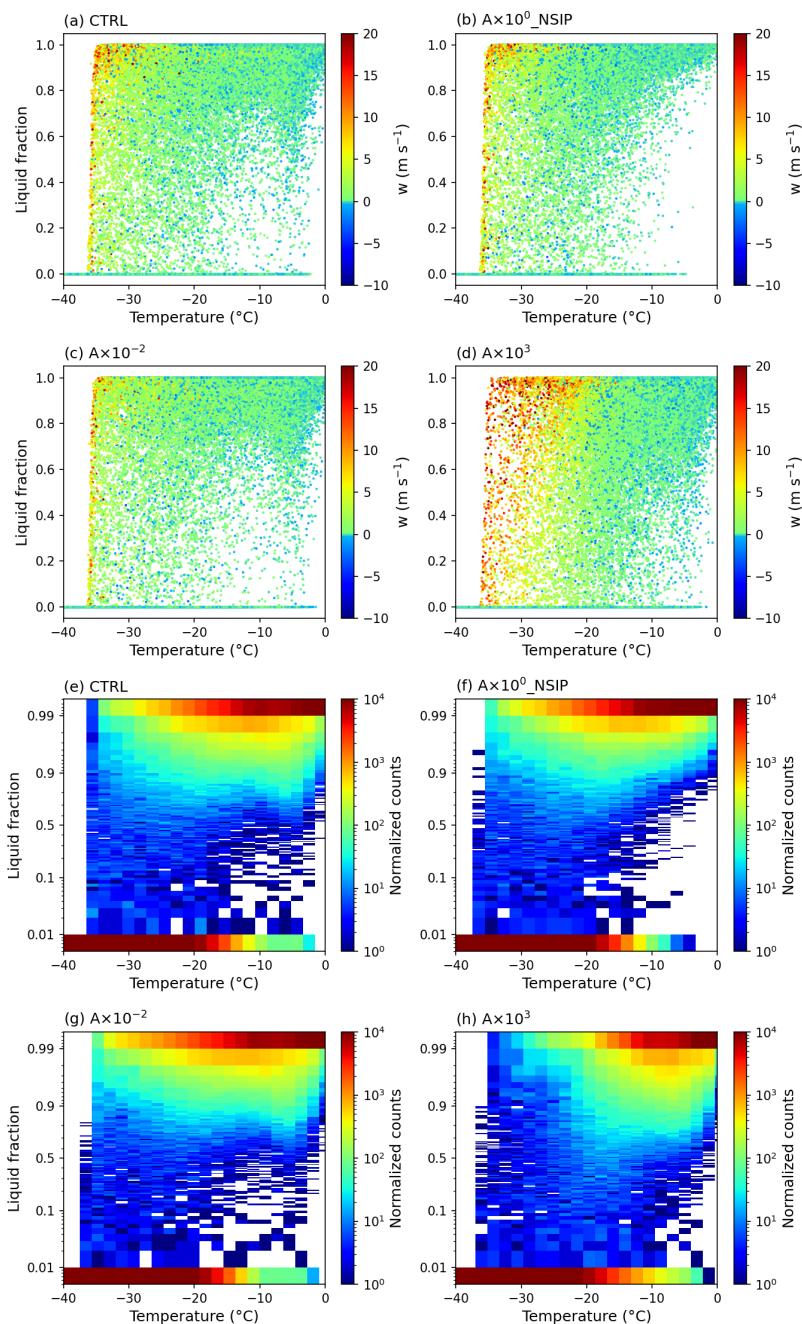




961

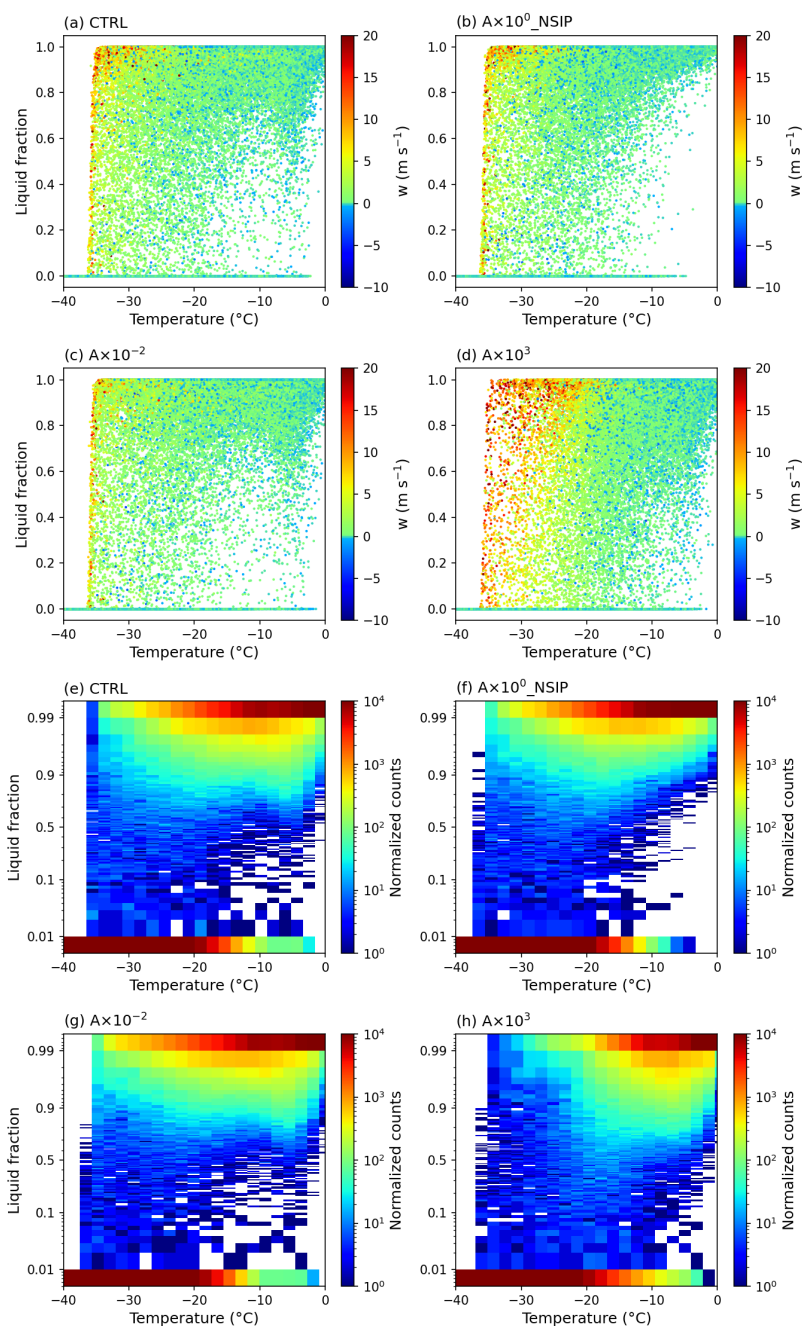
962 Figure 5: Spatial- and time-averaged (9:00~19:00) profiles of process rates of (a)  
963 heterogeneous freezing (immersion and deposition nucleation), (b) homogeneous  
964 freezing, (c) secondary-ice production (rime-splintering), (d) cloud droplets rimed  
965 with ice crystals, (e) rain droplets rimed with ice crystals, (f) collection between ice  
966 and ice. Unit is  $\text{g kg}^{-1} \text{s}^{-1}$ . The average mixed-phase layer ( $0\sim-38^\circ\text{C}$ ) is roughly in  
967 between 3.2 and 8.6 km. Unit is  $\text{g kg}^{-1} \text{s}^{-1}$ .

968



969

970 Figure 6: In-cloud supercooled liquid mass fraction distribution as a function of  
971 temperature (binned by  $1^{\circ}\text{C}$ ) between 9:00 and 19:00 (a-d) for the 4 cases ( $A \times 10^0$ ,  
972  $A \times 10^0$ \_NSIP,  $A \times 10^{-2}$ ,  $A \times 10^3$ ), the colour of points indicates the vertical wind velocity  
973 (unit,  $\text{m s}^{-1}$ ). 2-D histogram of in-cloud liquid mass fraction versus temperature (e-f).

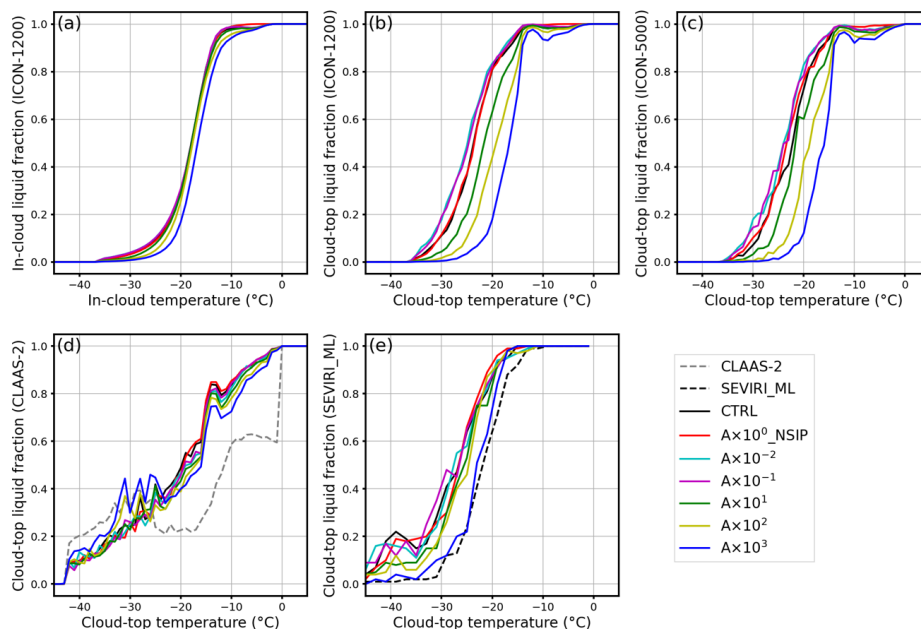


974

975 Figure 7: Cloud-top supercooled liquid mass fraction distribution as a function of  
976 temperature (binned by 1°C) between 9:00 and 19:00 (a-d) for the 4 cases ( $A \times 10^0$ ,  
977  $A \times 10^0_{NSIP}$ ,  $A \times 10^{-2}$ ,  $A \times 10^3$ ), the colour of points indicates the vertical wind velocity  
978 (unit, m s<sup>-1</sup>). 2-D histogram of cloud-top liquid mass fraction versus temperature (e-f).



979



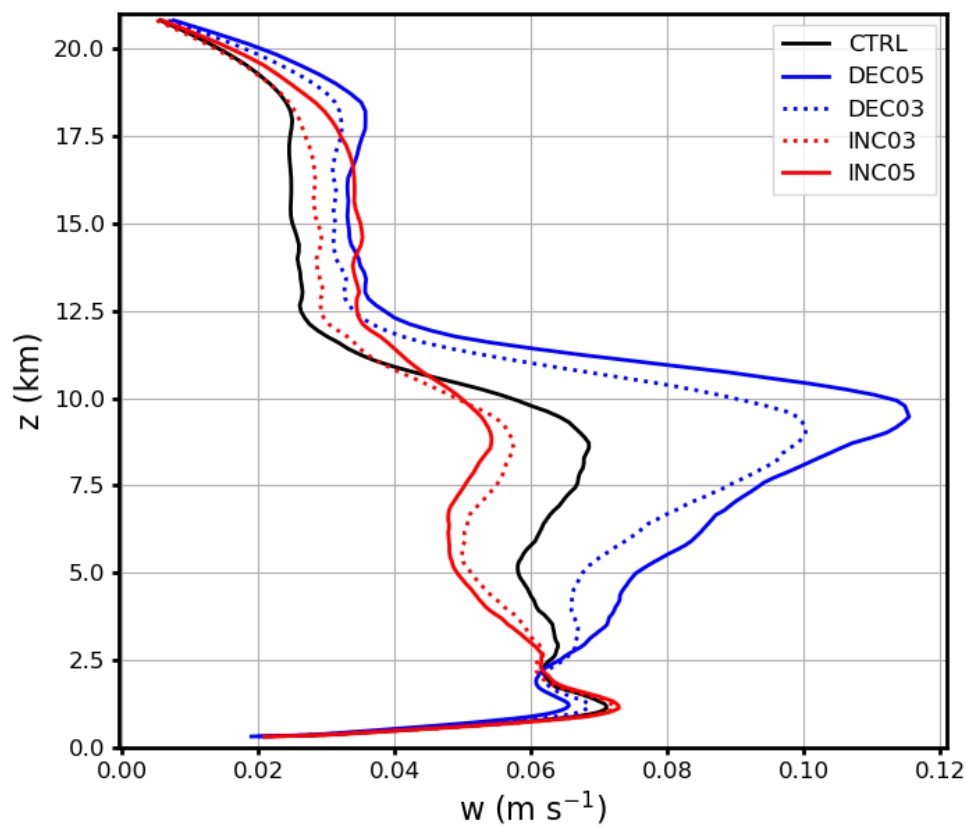
980

981 Figure 8: Liquid cloud pixel number fraction as a function of temperature from 9:00 to  
 982 19:00 UTC for the INP sensitivity experiments, (a) in-cloud fraction calculated from  
 983 simulations on ICON native grid (~1200 m), (b) cloud-top fraction calculated from  
 984 simulations on ICON native grid (~1200 m), (c) cloud-top fraction calculated from  
 985 simulations on SEVIRI's grid (~5000 m), (d) cloud-top fraction calculated by remote-  
 986 sensing retrieval algorithms to produce CLAAS-2 dataset, and (e) cloud-top fraction  
 987 calculated by remote-sensing retrieval software suite SEVIRI\_ML. The temperature  
 988 is binned by 1°C in (a), (b), (c), and (d), and by 2°C in (e).

989



990



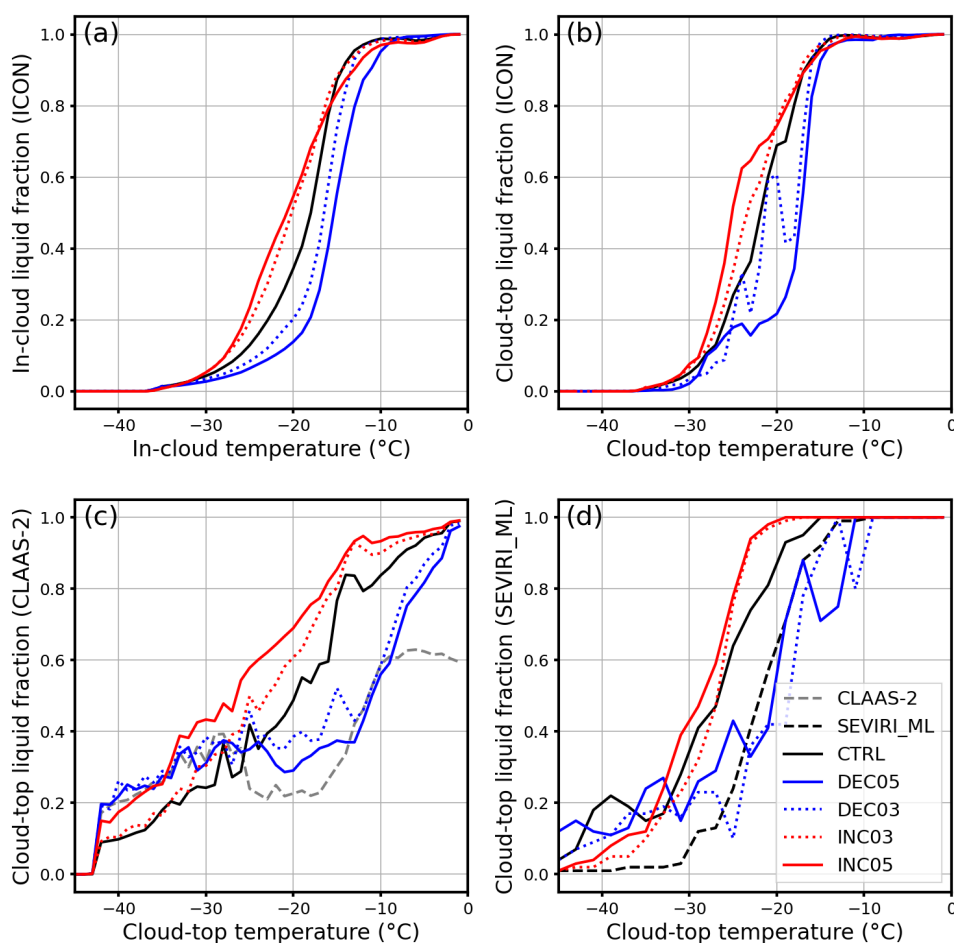
991

992 Figure 9: Spatial- and time-averaged (9:00~19:00) profiles of vertical velocities (w  
993 values  $\leq 0 \text{ m s}^{-1}$  are excluded).

994



995



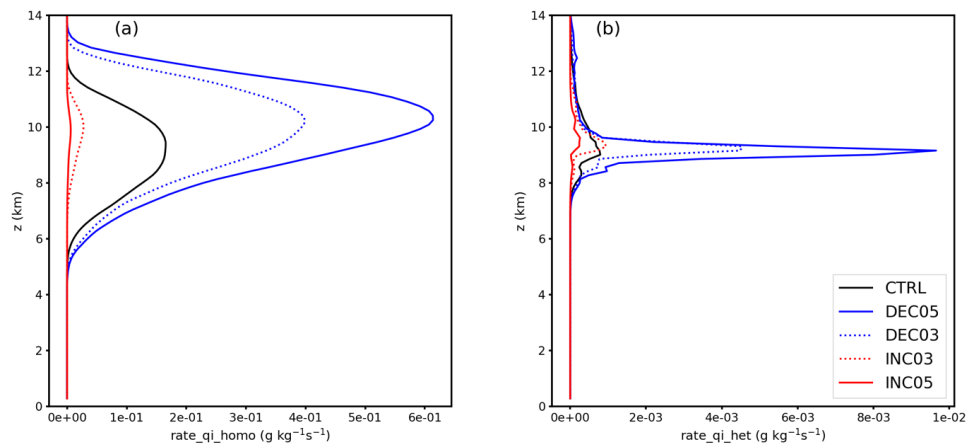
996

997 Figure 10: Liquid cloud pixel number fraction as a function of temperature from 9:00  
 998 to 19:00 for the thermodynamic sensitivity experiments, (a) in-cloud fraction  
 999 calculated directly from simulations, (b) cloud-top fraction calculated from directly  
 1000 simulated, (c) cloud-top fraction calculated by remote-sensing retrieval algorithms  
 1001 to produce CLAAS-2 dataset, and (d) cloud-top fraction calculated by remote-  
 1002 sensing retrieval software suite SEVIRI\_ML. The temperature is binned by 1°C in (a),  
 1003 (b), and (c), and by 2°C in (d).

1004



1005



1006

1007 Figure 11: Spatial- and time-averaged (9:00~19:00) profiles of process rates of (a)  
1008 homogeneous freezing, (b) heterogeneous freezing (immersion and deposition  
1009 nucleation) for cases with perturbed initial thermodynamic states. Unit is  $\text{g kg}^{-1} \text{s}^{-1}$ .

1010